Rational design and development of selective BRD7 bromodomain inhibitors and their activity in prostate cancer

Sandra C. Ordonez-Rubiano,[1] Chad A. Maschinot,[1] Sijie Wang,[1] Surbhi Sood,[1] Brayden P. Strohmier,[1] Alexander J McQuade,[1] Brian C. Smith,[3] Emily C. Dykhuizen.[12]*

[1]Department of Medicinal Chemistry and Molecular Pharmacology, College of Pharmacy, Purdue University. Robert Heine Pharmacy Building 575 Stadium Mall Drive West Lafayette, IN 47907

[2]Purdue Center for Cancer Research, College of Pharmacy, Purdue University. 201 S University St, West Lafayette, IN 47907.

[3]Department of Biochemistry, Program in Chemical Biology, Medical College of Wisconsin, Milwaukee, WI 53226, USA

*Corresponding author: Emily C. Dykhuizen, 201 S. University St. West Lafayette IN 47907, (765) 494-4706, edykhui@purdue.edu.

ABSTRACT

Bromodomain-containing proteins are readers of acetylated lysine and play important roles in cancer. Bromodomain-containing protein 7 (BRD7) has been implicated in multiple malignancies; however, there are no selective chemical probes to study its function in disease. Using crystal structures of BRD7 and BRD9 bromodomains (BDs) bound to BRD9-selective ligands, we identified a binding pocket exclusive to BRD7. We synthesized a series of ligands designed to occupy this binding region and identified two BRD7-selective inhibitors, 1-78 and 2-77, that bind with nanomolar affinity to the BRD7 BD. Our binding mode analyses indicate that these ligands occupy a uniquely accessible binding cleft in BRD7 and maintain key interactions with the asparagine and tyrosine residues critical for acetylated lysine binding. Finally, we validated the utility and selectivity of the compounds in cell-based models of prostate cancer.

INTRODUCTION

Chromatin remodelers are multi-subunit epigenetic regulators that modulate the accessibility of DNA.[14] The BRG1-associated factors (BAF) complexes function as ATP-dependent chromatin remodelers and consist of three biochemically distinct complexes: canonical BAF (cBAF), polybromo-associated BAF (PBAF), and GLTSCR1/like-containing BAF (GBAF or ncBAF) (**Figure 1A**).[15–18] All three types of BAF complexes share the ATPase and several core subunits, but also contain unique subunits. BAF complexes are the most frequently mutated chromatin remodeling complex in cancer, and different subunits, in cooperation with the catalytic subunits BRM and BRG1, play crucial roles in regulating chromatin accessibility.[19–22] Multiple compounds have been developed to target BAF complex subunits, including small molecules and proteolysis targeting chimeras (PROTACs); however, most of the subunits have yet to be explored as targets in disease. [23–40]

In the human proteome, there are forty-six bromodomain-containing proteins that are predicted to recognize acetylated Lys in proteins, most commonly histones.[1] Bromodomains (BDs) are therapeutic targets in multiple diseases, and several BD inhibitors are currently under phase I, II, or III clinical studies (www.clinicaltrials.gov).[41] In the BAF complexes, unique bromodomain-containing subunits, such as bromodomain-containing protein 7 (BRD7) in PBAF, or bromodomain-containing protein 9 (BRD9) in GBAF, are likely to mediate subcomplex specific function. BRD7 contains a single BD in its structure that belongs to BD family IV (**Figure 1B**). BRD7 has been reported to be involved in advancing of several types of tumors such as nasopharyngeal carcinoma, osteosarcoma, and colorectal, breast, ovarian, and prostate cancer (PCa), as well as in the regulation of immune response.[3–13] Although BRD7 has been implicated in several disease-related roles, there are currently no selective chemical probes to study its potential as a therapeutic target.
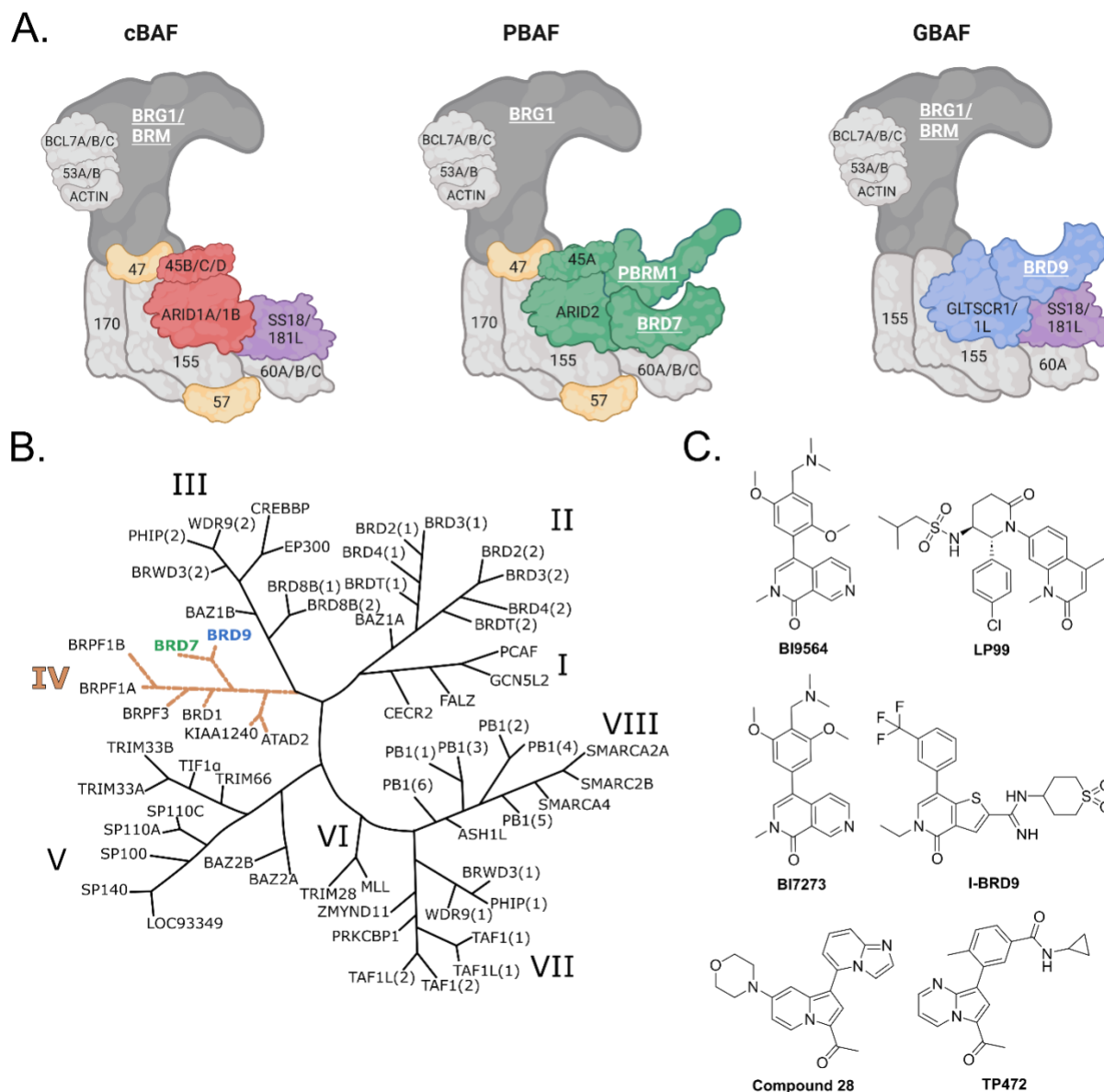
Figure 1. A. Composition of the three BAF subcomplexes. In dark grey: catalytic subunit; in light gray: subunits shared by all complexes; in yellow: subunits shared by cBAF and PBAF; in purple: subunits shared by BAF and GBAF; in red: cBAF unique subunits; in green: PBAF unique subunits; in blue: GBAF unique subunits. Bromodomain-containing proteins are labeled in underlined white bold font. **B.** Phylogenetic BD tree as described by Filippakopoulos et al. (2012).[1] **C.** Reported BRD7/9 ligands with selectivity for BRD9 over BRD7.

Here we report the development of BRD7-selective chemical probes from ligands selective for BRD9 (**Figure 1C**), the closest BD homolog of BRD7 (73.2% sequence identity between the BDs) (**Figure S1**). We used structure-based drug design and *in silico* screening to discover two closely related BRD7-selective inhibitors with nanomolar affinity for BRD7. We further validated their efficacy and selectivity in BRD7-dependent PCa cell lines.
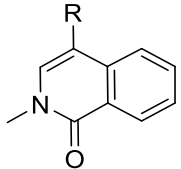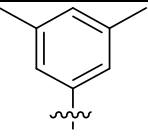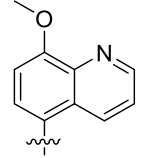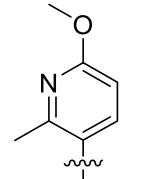
RESULTS AND DISCUSSION

Rational design and synthesis of BRD7 BD probes. The BRD9 BD inhibitor BI9564 also binds to the closely related BRD7 BD, although with lower affinity (K_d values of 19 nM and 117 nM, respectively).[26] BI9564 forms two hydrogen bonds with BRD9[Asn216], a water-mediated hydrogen bond with BRD9[Tyr168], a π-π interaction with
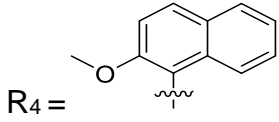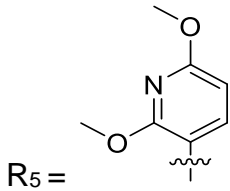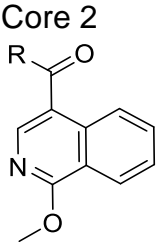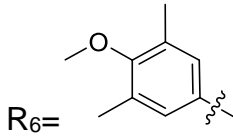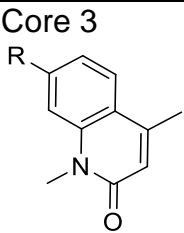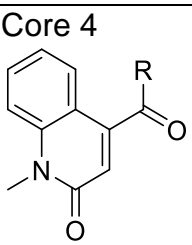
BRD9[Tyr222], a C-H π-interaction with BRD9[Ile164], and a T-stacking interaction with BRD9[Phe160].[26] Although BI9564 also binds to the BRD7 BD, the binding affinity is reduced, potentially due to differences in van der Waals interactions or entropic costs associated with the increased flexibility of BRD7 BD in solution.[26,27] To exploit structural differences between the two BDs to develop BRD7-selective inhibitors, we compared the deposited structures of the BRD7 BD (PDB: 5MQ1) and BRD9 BD (PDB: 5F1H) bound to BI9564. We identified an open hydrophobic region adjacent to the acetylated Lys binding pocket in BRD7 BD that is unavailable in BRD9 BD due to the Phe side chain orientation (**Figure 2**). To achieve selectivity for BRD7 over BRD9, we designed a library of ligands that would accommodate the acetylated Lys binding pocket similar to known BRD7/9 ligands but extend into this BRD7-specific binding pocket. The thirteen library members contain one of four common cores found in known BRD7/9 ligands and were synthesized in one or two steps from commercially available building blocks. The compounds are summarized in **Table 1** and **Scheme 1**.
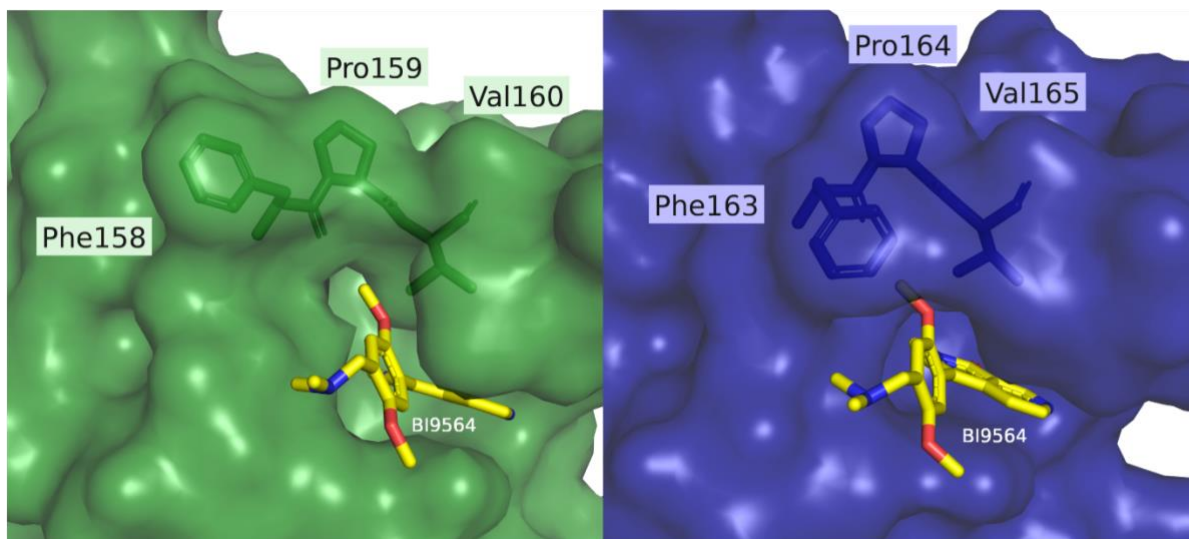
Figure 2. Comparison of the BD binding pockets of BRD7 (**left**, green; PDB: 5MQ1) and BRD9 (**right**, blue; PDB: 5F1H) crystallized with BI9564, a known BRD7/9 dual inhibitor. The comparison suggests that BRD7 may allow for a larger hydrophobic moiety than BRD9. Figure created with PyMOL.

Table 1. Structure of the designed inhibitors classified into four different groups.

Group	Compound	R
Core 1	**1-38**	$R_1 =$
	1-70	$R_2 =$
	1-79	$R_3 =$

	2-79	 $R_4 =$
	2-88	 $R_5 =$
Core 2 	**2-49**	R_1
	2-63	 $R_6 =$
Core 3 	**1-75**	R_1
	1-78	R_3
	2-77	R_5
	2-81	R_4
Core 4 	**2-70**	R_1
	2-71	R_6

Synthesis of core option 1 group
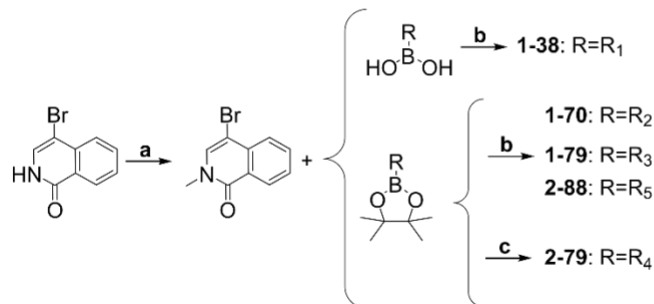
Synthesis of core option 2 group
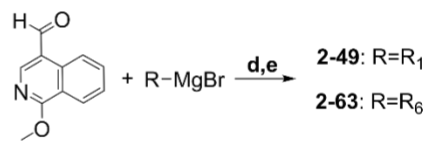
Synthesis of core option 3 group
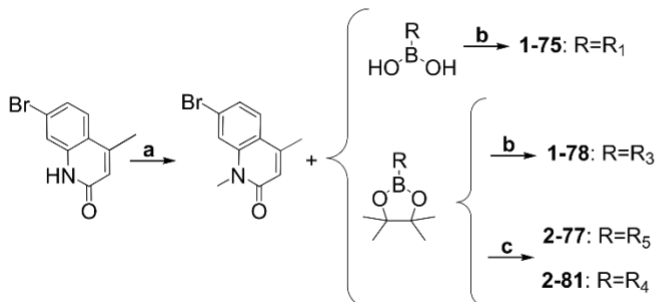
Synthesis of core option 4 group
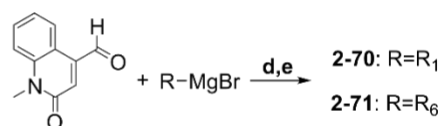
Scheme 1. Reagents and conditions for the synthesis of the designed BRD7 inhibitors. (a) NaH, DMF (anhydrous), CH$_3$I at 0 °C warm to rt, 16 h; (b) Pd(dppf)Cl$_2$, Cs$_2$CO$_3$, DMF (anhydrous), reflux, 16 h; (c) Pd(dppf)Cl$_2$, Cs$_2$CO$_3$, 1,4-dioxane (anhydrous), reflux, 48 - 72 h; (d) aryl aldehyde in THF at 0 °C, Grignard reagent added over 10 minutes, then quenched; (e) pyridinium dichromate, DCM.

Thermal shift assay (TSA) to evaluate stability of the BRD7 and BRD9 BDs when bound to the ligands. We performed a TSA based on differential scanning fluorimetry to identify compounds that stabilize the BDs and increase the melting temperature (T$_m$) upon binding. We tested all 13 synthesized compounds along with the dual BRD7/9 inhibitor BI7273, which has a better BRD7 binding profile than BI9564, as a control.[26] BI7273 showed binding and stabilization of BRD9 and BRD7 (**Figure 3**). Of the compounds with core 1, 1-38 stabilized and increased the T$_m$ of BRD7 BD and BRD9 BD, while 2-88 stabilized only BRD9 BD. Of the compounds with cores 2 and 4, none increased the T$_m$ of either of BD. Of the compounds with core 3, 1-78 and 2-77 increased the T$_m$ of BRD7 BD but not BRD9 BD. Therefore, the results from the TSA suggested that 1-78 and 2-77 could be BRD7-selective binders.
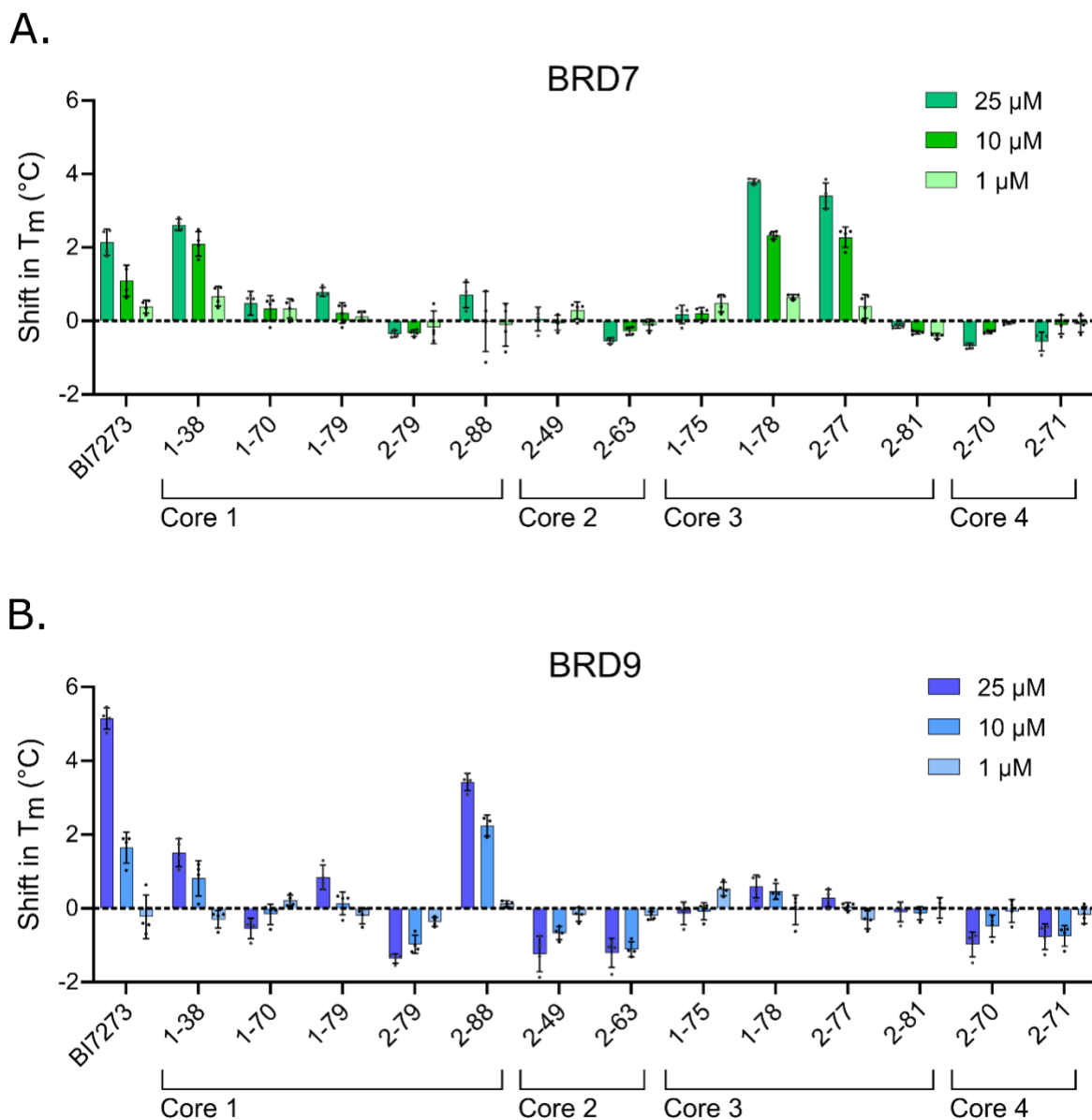
Figure 3. Results from the TSA. Each HIS-tagged BD (**A.** BRD7 BD or **B.** BRD9 BD) was incubated with the compounds at 25, 10 or 1 µM. The T_m of the proteins was calculated based on differential scanning fluorimetry readings at increasing temperatures from four replicates using nonlinear least squares fit on GraphPad Prism 9. The shift in T_m was calculated with respect to vehicle control.

Competitive fluorescence polarization (FP) assay shows 1-78 and 2-77 are selective for BRD7 over BRD9. To further characterize the compounds, we developed a fluorescent labeled probe, BI-FAMa, that consists of BI7273, a 4-carbon linker, and a fluorescein (FAM) label for use in a competitive FP assay (**Figure 4A**). We characterized BI-FAMa binding to the BRD7 and BRD9 BDs and calculated a K_d of 510 nM for BRD9 and a K_d > 10 µM for BRD7 (**Figure 4B and 4C**). For successfully carrying out a competitive FP assay with BRD7, a probe with a lower K_d value was required to saturate the system at a soluble protein concentration. With this in mind, we developed BI-FAMb with a 6-carbon linker to give more flexibility to the molecule (**Figure 4D**). This fluorescent probe had a K_d of 705 nM for BRD7 and 24 nM for BRD9, which was more comparable to the reported K_d value for BI7273, and suitable for a competitive FP assay (**Figure 4E and 4F**). For the competitive assay we used a concentration of 5 µM and 0.25 µM of BRD7 BD and BRD9 BD, respectively, to achieve approximately 90% saturation of the FP signal observed in the direct binding experiment. We tested the compounds and BI7273

as a control in decreasing doses starting at 25 μM. Four of the inhibitors bound to both proteins: 1-38 and 2-88 from core 1 and 1-78 and 2-77 from core 3 (**Figure S2 and S3**). Using the IC_{50} values obtained from the competition assay, and the apparent K_d of each protein for BI-FAMb, we estimated K_i values for each of the compounds employing the equation reported by Cer et al. (2009) (explained in detail in the Experimental section) (**Table 2**).[42] As expected, the calculated K_i of BI7273 was almost 20-fold lower for BRD9 than for BRD7. In addition, compounds 1-38 and 2-88 showed selectivity for BRD9 over BRD7, and 1-78 and 2-77 showed selectivity for BRD7 over BRD9, which aligns with the results obtained from the TSA. The results from the FP assay further supported 1-78 and 2-77 as BRD7-selective inhibitors.
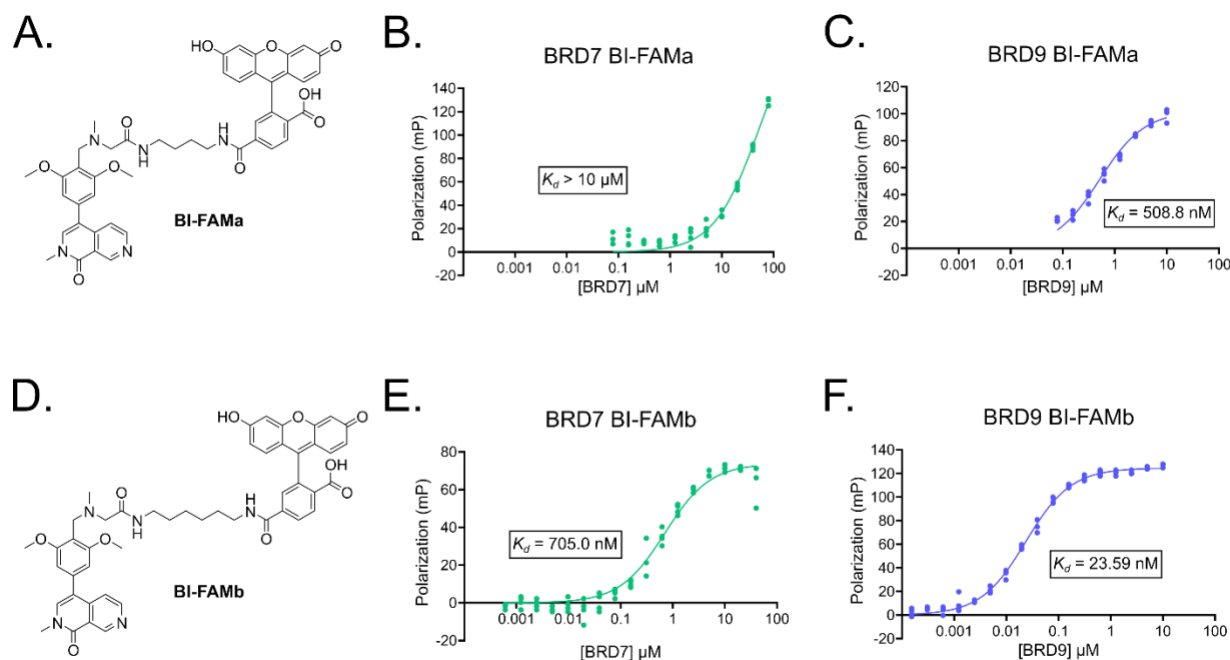
Figure 4. **A.** Structure of BI-FAMa. **B.** Fluorescence polarization of BI-FAMa with increasing concentrations of BRD7 and **C.** BRD9. **D.** Structure of BI-FAMb. **E.** Fluorescence polarization of BI-FAMb with increasing concentrations of BRD7 and **F.** BRD9. Approximate K_d values were obtained from nonlinear "One Site - Specific binding" fit analyses on GraphPad Prism 9.

Table 2. Binding affinity of inhibitors to BRD7 and BRD9.

Compound	$IC_{50 \text{ BRD7}}$ (μM)[a]	$K_{i \text{BRD7}}$ (μM)[b]	$IC_{50 \text{ BRD9}}$ (μM)[a]	$K_{i \text{BRD9}}$ (μM)[b]
BI7273	2.81	0.34	0.22	0.018
1-38	8.09	0.98	3.97	0.34
1-78	1.61	0.20	2.69	0.23
2-77	18.97	2.30	310	27
2-88	2.86	0.35	1.52	0.13

Binding mode analysis of 1-78 and 2-77. BRD7/9 inhibitors have a pharmacophore that mimics an acetylated Lys and forms a hydrogen bond with the highly conserved Asn in the BD binding pocket (BRD7[Asn211], BRD9[Asn216].[27,43] More recent crystal structures of BRD9 BD and BRD7 BD indicate that the aromatic systems in BI7273, BI9564, I-BRD9, TP-472, and Bromosporine form π-π interactions with BRD7[Tyr217] or BRD9[Tyr222] In these structures, the hydrophobic pocket in BRD7 (**Figure 2, left**) is also available in BRD9, indicating that these compounds achieve selectivity through an alternate mechanism than originally proposed (**Figures 5A, 5B, and S4**).[27,43] Using pregenerated receptor grids, we docked 1-78 and 2-77 into the structures of BRD7 and BRD9 BDs crystallized with BI7273 (**Figure 5A**, PDB: 6V1E; and **Figure 5B**, PDB: 5EU1, respectively). 2-77 interacts with BRD7 BD to maintain the same key interactions found between BI7273 and BRD7[Asn211] and BRD7[Tyr217] (**Figure 5C**). BRD9 BD, however, cannot accommodate the core of 2-77 inside the pocket. Instead, the software docks 2-77 into the BRD9 BD binding pocket via the pyridine moiety of the molecule, such that the aromatic ring forms a π-π interaction with BRD9[Tyr216], and a hydrogen bond can be formed between the oxygen of the *para*-methoxy group and BRD7[Asn211] (**Figure 5D**). In contrast, the docking shows 1-78 maintains the π-π interactions between the pharmacophore and both BRD7[Tyr217] and BRD9[Tyr216]; however, to accommodate the steric bulk of 1-78 in BRD9 BD, the key hydrogen bond between the amide oxygen and BRD9[Asn216] is not maintained (**Figure 5E and 5F**).
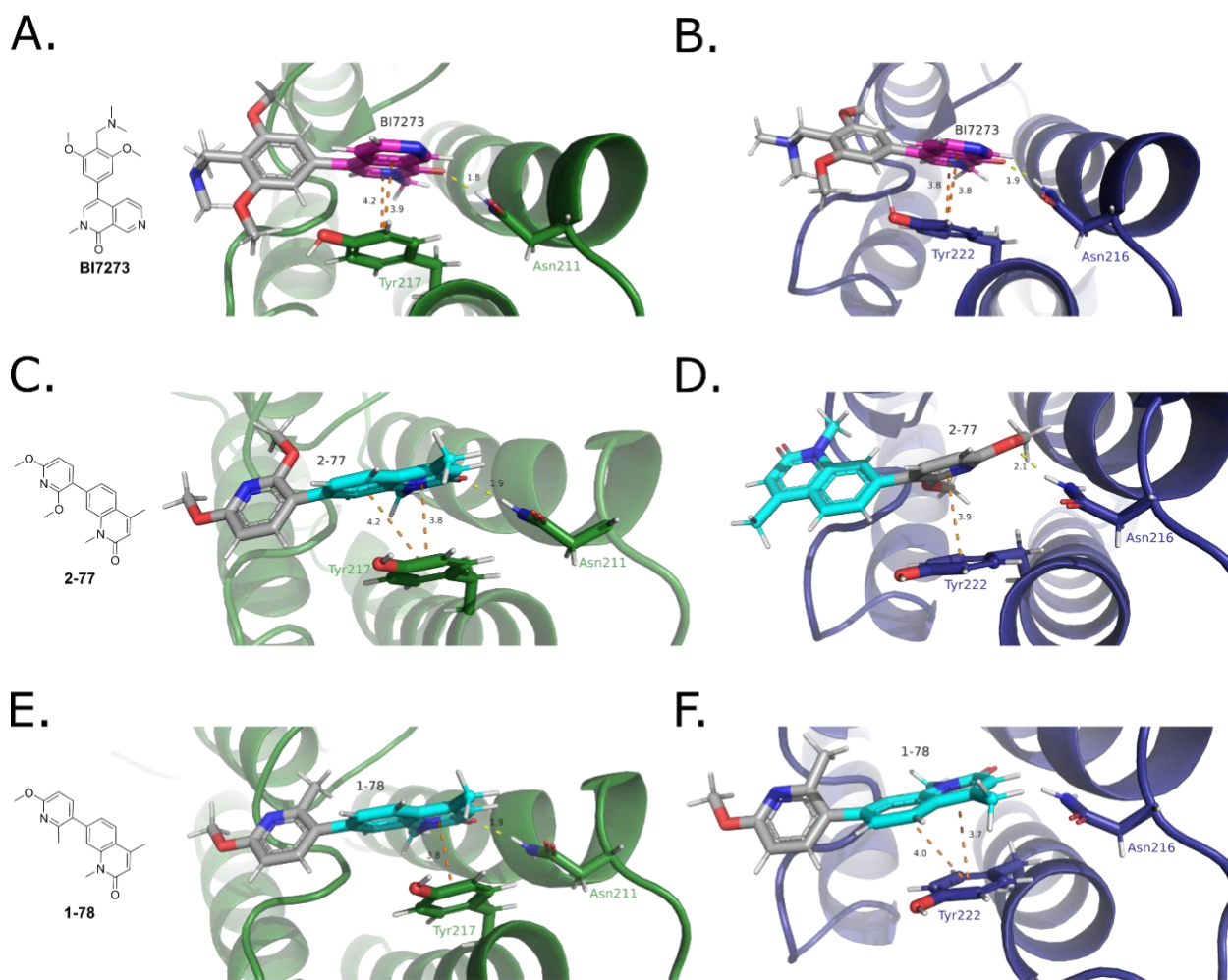
Figure 5. Binding mode analysis of compounds docked against BRD7 BD (PDB: 6V1E) and BRD9 BD (PDB: 5EU1) performed in the Schrödinger® Maestro suite. BI7273 was docked into **A.** BRD7 BD (green) and **B.** BRD9 BD (blue). 2-77 was docked into **C.** BRD7 BD (green) and **D.** BRD9 BD (blue). 1-78 was docked into **E.** BRD7 BD (green) and **F.** BRD9 BD (blue). Shown in sticks: the conserved Asn involved in the hydrogen bond and the Tyr involved in the π-π interactions. In magenta in A and B: the core of BI7273. In cyan in C to F: the core of 2-77 and 1-78. π-π interactions are depicted in orange dotted lines. Hydrogen bonds are depicted in yellow dotted lines. Distance of the interactions given in Å. Figures created in PyMOL.

BROMO*scan*™ and *bromoKd*ELECT profiling of 1-78 and 2-77. To evaluate the selectivity profile over 40 distinct BDs, we screened 1-78 and 2-77 in the BROMO*scan*™ panel (Eurofins DiscoverX Corp.). Both 1-78 and 2-77 showed selectivity for BRD7 over BRD9 at a 2 μM concentration (**Figure 6A**). In a separate experiment, we also tested compounds with activity against both BRD7 and BRD9 in the TSA (1-38) (**Figure 3A**) or with weak binding to BRD7 (2-81) in the BROMO*scan*™ and observed no binding to other bromodomains. (**Figure S5**). We additionally used the *bromoKd*ELECT platform (Eurofins DiscoverX Corp) to evaluate the binding affinity of the compounds for BRD7 BD. The results showed that 1-78 and 2-77 have a K_d average of 290 nM and 340 nM for BRD7, respectively (**Figure S6**). Unexpectedly, both compounds show off-target binding for bromodomain and PHD finger-containing protein 1 (BRPF1) in the BROMO*scan*™ even though the sequence identity between the BDs of BRFP1 and BRD7 is only 38% (**Figure S1**). Some BRPF1 inhibitors reported in literature share a core similar to that of 1-78 and 2-77, such as NI-48, with differences in the position of the methyl group with respect to the lactam ring and the position at which the R-group binds to the core (**Figure 6B, left**).[44] We analyzed the interactions between NI-48 and the BRPF1 BD (PDB: 5T4V), and found that the binding mode is similar to that of our compounds (**Figure S7**). The oxygen of the lactam ring of NI-48 also forms a hydrogen bond with the conserved Asn BRPF1[Asn708], and the core of the compound forms two π-π interactions with BRPF1[Phe714]. Additionally, the R-group of NI-48 forms an edge-to-face π-π interaction with BRPF1[Phe714] allowed by the length and flexibility of the chain that connects the R-group to the core.

The BROMO*scan*™ is a competitive binding assay and not a direct binding assay; therefore, it is difficult to assess from the BROMO*scan*™ alone how well our BRD7 inhibitors bind to BRPF1. For this reason, we also tested our inhibitors against the BD of BRPF1 using TSA. As a control for this assay we employed GSK-5959, a BRPF1-selective inhibitor with a different bicyclic system and an IC$_{50}$ of 98 nM (**Figure 6B, right**).[45] GSK-5959 did not bind to BRD7 or BRD9 but stabilized BRPF1 at concentrations as low as 1 μM (**Figure 6C**).[45] In contrast, 1-78 was the only BRD7 inhibitor to display even modest stabilization of BRPF1 at the highest concentration (25 μM). Even though the compounds can compete with non-selective ligands for BRPF1 binding in the BROMOscan™, they are not potent enough to stabilize the BRPF1 BD *in vitro* at concentrations that stabilize the BRD7 BD.

To better understand why the compounds do not stabilize BRPF1 BD to the same extent as BRD7 BD, we evaluated their binding mode *in silico*. We docked 1-78, 2-77, and GSK-5959 into the binding pocket of the BRPF1 BD crystallized with NI-48 (PDB: 5T4V) (**Figure S8**). As expected, the core of GSK-5959 forms a hydrogen bond with the conserved Asn in BRPF1 (BRPF1[Asn708]) and a π-π interaction with BRPF1[Phe714], which is the gatekeeper of the binding pocket in the BRPF1 BD instead of the conserved Tyr in BRD7 and BRD9 (BRD7[Tyr217] and BRD9[Tyr222], respectively). Even though 1-78 fits in the binding pocket, it lacks the critical hydrogen bond with BRPF1[Asn708], which could explain the reduced BRPF1 stabilization by 1-78 in the TSA. Similar to what we observed when docking 2-77 into BRD9, BRPF1 cannot accommodate 2-77 in its binding pocket while maintaining critical binding interactions.

After inspecting the binding mode of 1-78 and 2-77 to BRD7, BRD9 and BRPF1 in the docking experiments (**Figures 2C and 2E, 2D and 2F, and S8B and S8C, respectively**), we observed that the structural feature of the proteins that is providing the steric hinderance is not the availability of a hydrophobic pocket. Instead, the width and flexibility of the section that bridges the inner and outer regions of the binding pocket appear to be sterically restricting the binding of the compounds. In an unliganded state, the bridge in BRD7 is in an open disposition

allowing the entrance of small molecules, which closes once the π-π interaction is formed between the core of the inhibitors and BRD7^{Tyr217}. The position of BRD9^{Tyr222}, however, appears to restrict the bridge once it closes and prevents binding to rigid small molecules that cannot easily rotate to adapt to the constricted space, such as 1-78 and 2-77. Similarly, in BRPF1 the entrance is restricted by BRPF1^{Phe714} but is less narrow than in BRD9, which could explain why we still see some competition in the BROMO*scan*^{TM} platform. To further explore why BRD9 and BRPF1 cannot bind to 2-77, we aligned the pose of 2-77 bound to BRD7 with the binding pockets of BRD9 and BRPF1 (**Figure 6D and 6E, 6F and 6G, and 6H and 6I for BRD7, BRD9, and BRPF1, respectively**). The R-group of 2-77 occupies the hydrophobic region in BRD7 without any steric hindrance (**Figure 6E**); however, the R-group clashes with the binding pocket of BRD9 and BRPF1 (**Figure 6G and 6I, respectively**), explaining the selectivity we observed in the *in vitro* assays.

In all, we have developed two compounds, 1-78 and 2-77, which are selective for the BRD7 BD *in vitro*. To validate their use as tools to study the function of BRD7 we next tested them *in cellulo*.
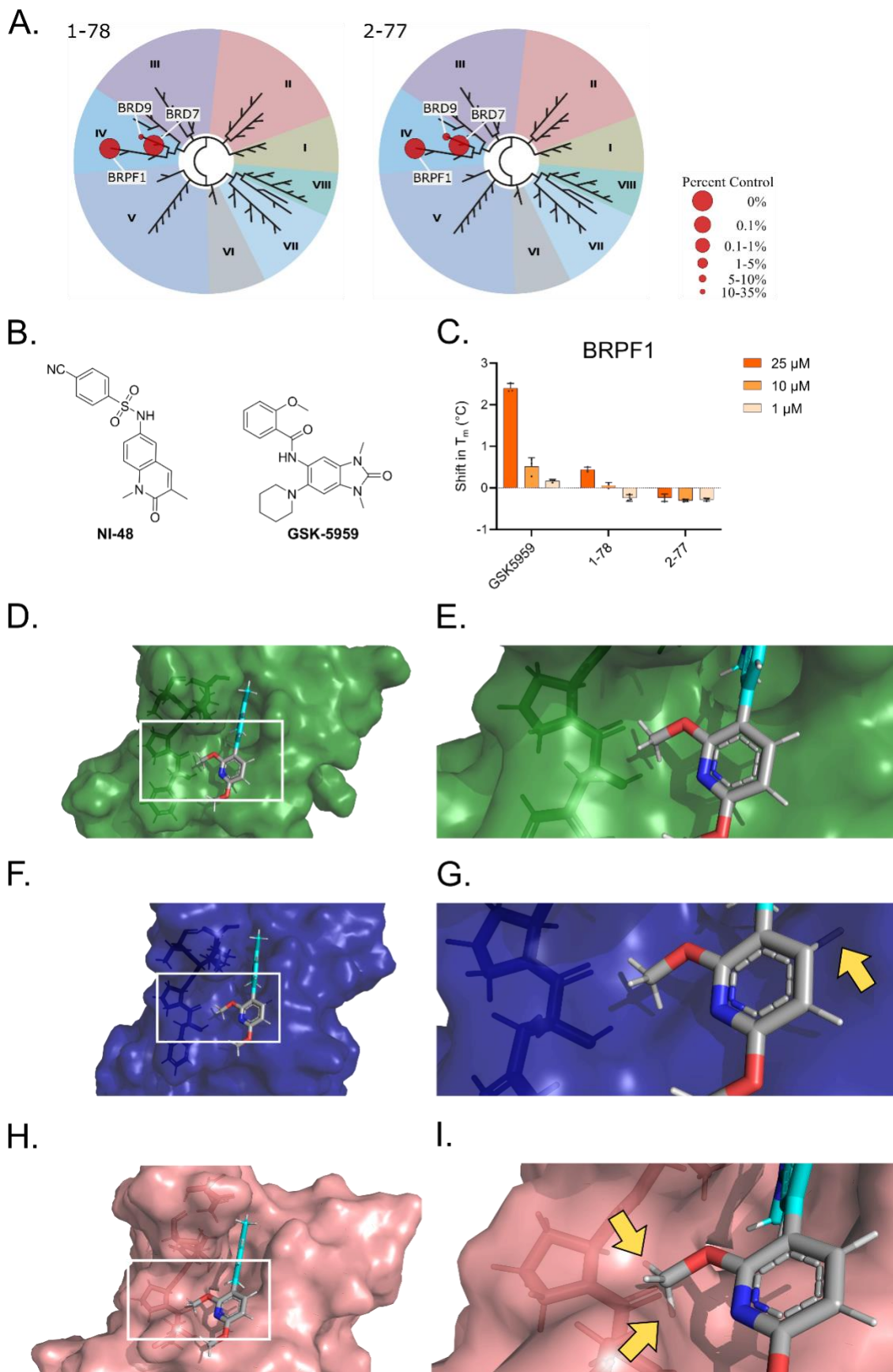
Figure 6. A. TREEspot™ interaction maps for 1-78 and 2-77 screened in the BROMO*scan*™ platform. The results for binding interactions for the compounds are reported as % of control (DMSO). **B.** Structures of the BRPF1

inhibitors NI-48 and GSK-5959. **C.** Results from the TSA using HIS-tagged BRPF1 and compounds at 25, 10 or 1 µM. The T_m of the proteins in the different conditions was calculated based on differential scanning fluorimetry readings at increasing temperatures from four replicates using nonlinear least squares fit on GraphPad Prism 9. The shift in T_m was calculated with respect to the vehicle. **D.** 2-77 docked against BRD7, showing the surface of the protein and depicting the amino acids involved in the hydrophobic region right outside the binding pocket as sticks. **E.** Zoomed in region indicated in D. **F.** The binding pose of 2-77 docked against BRD7 aligned to the binding pocket of BRD9, showing the surface of BRD9 and depicting the amino acids involved in the hydrophobic region right outside the binding pocket as sticks. **G.** Zoomed in region indicated in F. **H.** The binding pose of 2-77 docked against BRD7 aligned to the binding pocket of BRPF1, showing the surface of BRPF1 and depicting the amino acids involved in the hydrophobic region right outside the binding pocket as sticks. **I.** Zoomed in region indicated in H. Yellow arrows in G and I indicate where 2-77 clashes with the binding pocket of BRD9 and BRPF1, respectively. Figures created with PyMOL.

NanoBRET[TM] target engagement with BRD7 and BRD9 BDs. To evaluate the compounds in a cell-based model we performed a NanoBRET assay to assess intracellular BD engagement by the compounds. To do so we expressed the BDs of BRD7 and BRD9 fused with luciferase in HEK293T cells and first incubated them with increasing concentrations of NanoBRET[TM] BRD Tracer-02 (provided by Promega) designed to generate BRET when bound to the target BDs (**Figure S9**). Using these binding profiles, we selected 0.4 µM as the tracer concentration for the NanoBRET[TM] assay. We then performed a competition assay by treating the cells with increasing concentrations of 1-78, 2-77, and BI7273. As expected, BI7273 had a lower IC_{50} for BRD9 (24 nM) than for BRD7 (1.21 µM) (**Figure 7A**). When treating the cells with 1-78 and 2-77, we observed a lower IC_{50} for BRD7 (818 nM and 1.48 µM, respectively) than for BRD9 (3.29 µM and 2.47 µM, respectively), indicating that the compounds were selective for BRD7 BD over BRD9 BD *in cellulo* (**Figures 7B and 7C**).
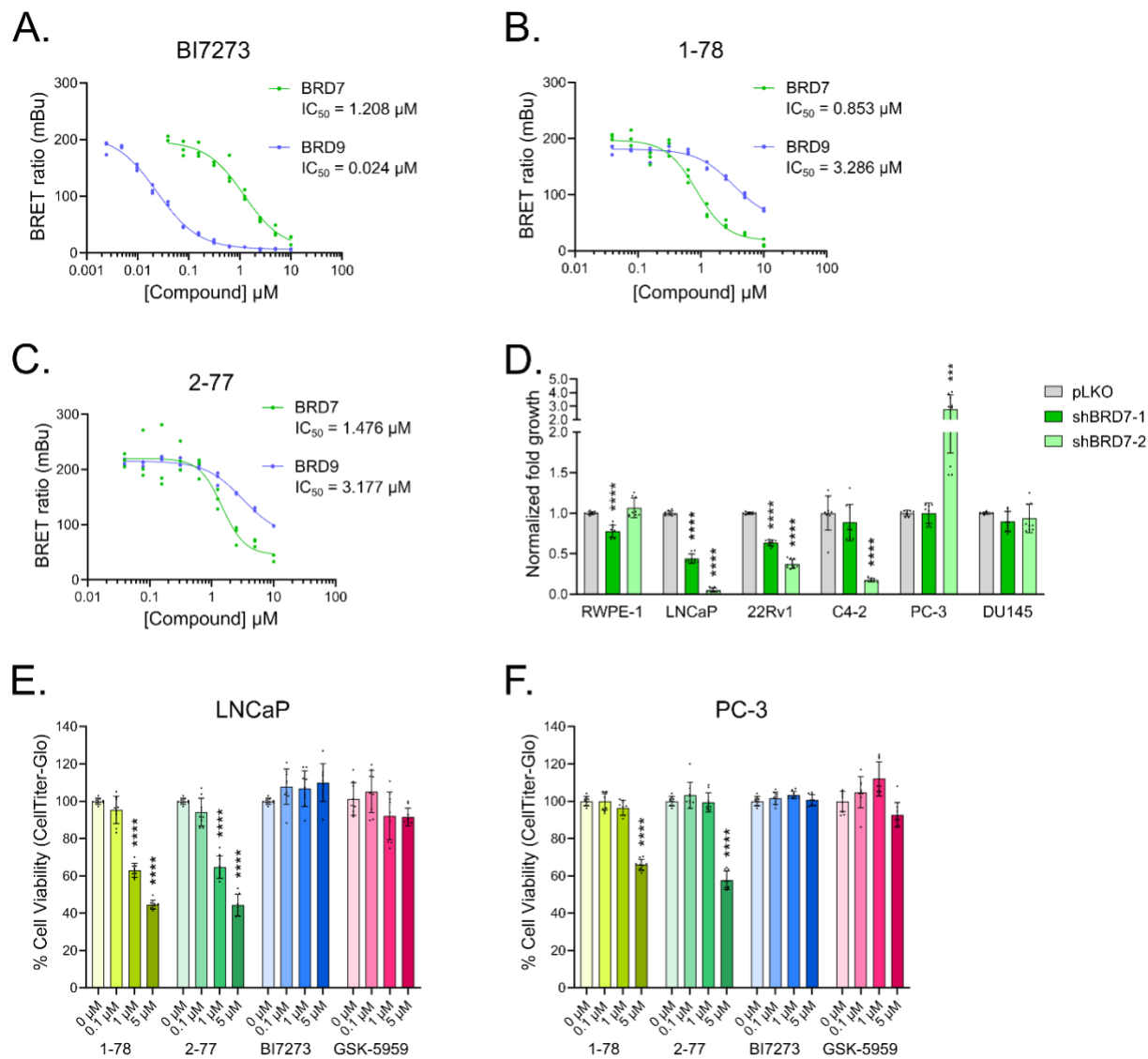
Figure 7. *In cellulo* assays. **A.** NanoBRET assay results treating HEK293T cells for 2 hours with increasing concentrations of BI7273, **B.** 1-78, and **C.** 2-77. The BRET ratio in milliBRET units (mBu) was calculated as described in the Experimental section. The IC$_{50}$ was calculated using nonlinear least squares fit on GraphPad Prism 9. **D.** Normalized fold increase in growth after 4 days of incubation of RWPE-1, LNCaP, 22Rv1, C4-2, PC-3 and DU145 cells in which BRD7 has been knocked down with two different constructs. Cell viability was measured with a CellTiter-Glo® Luminescent Cell Viability Assay on day 0 and day 4. Includes 3 replicates each from 3 separate experiments. **E.** LNCaP and **F.** PC-3 viability after 4 days of incubating the cells with compounds 1-78 and 2-77, the BRD7/9 inhibitor BI7273, and the BRPF1 inhibitor GSK-5959. Includes 3 replicates each from 3 separate experiments. Cell viability was measured employing a CellTiter-Glo® Luminescent Cell Viability Assay. Error bars represent s.d. n = 9. Statistical significance was determined using multiple t-tests with respect to empty vector or vehicle, respectively. * $p = < 0.05$, ** $p = < 0.01$, *** $p = < 0.001$, **** $p = < 0.0001$.

BRD7 inhibitors do not displace BRD9 from chromatin. PBAF contains a total of eight BDs across three separate subunits. We found previously that a single BD mutation in (or even full deletion of) the polybromo-1 (PBRM1) PBAF subunit can slightly reduce but not abrogate PBAF global chromatin association.[17,46,47] In contrast, a single BD mutation or inhibition of the BRD9 subunit completely dissociates GBAF from chromatin.[17,48] To determine whether our BRD7 inhibitors can displace BRD9 from chromatin at cellularly active concentrations, we performed a cell fractionation assay. We treated HEK293T cells with 10 µM of the compounds

or DMSO and collected nuclear soluble and chromatin insoluble fractions. Using western blotting, we evaluated the relative amount of BRD9 still bound to chromatin after inhibitor treatment. I-BRD9 treatment significantly reduced BRD9 from chromatin while 1-78 and 2-77 did not, indicating that while the NanoBRET assay detects some off-target binding to BRD9 at 10 µM, it is not sufficient to inhibit BRD9 chromatin binding (**Figure S10**).

BRD7 inhibition reduces cell proliferation in PCa cell-based models. PCa is the second leading cause of death and the most frequently diagnosed cancer in men in the US, with 34,700 associated deaths and 288,300 new cases estimated for 2023.[49] BRD7 has been identified as a prognostic marker and facilitator of PCa progression.[8–10] Depletion of *BRD7* reduces expression of testosterone-response genes in HAP1 cells;[20] however, the therapeutic potential of targeting BRD7 in PCa has not been explored, in part due to a lack of chemical tools.

PCa can be classified as either hormone naïve or castration resistant, and either androgen receptor (AR)-positive or AR-negative.[50] In our studies, we employed six different cell lines to model the disease: RWPE-1 (normal prostate epithelial cells), LNCaP (hormone naïve, AR-positive PCa cells), 22Rv1 (castration resistant, AR-positive PCa cells), C4-2 (castration resistant, AR-positive PCa cells), PC-3 (castration resistant, AR-negative PCa cells), and DU145 (castration resistant, AR-negative PCa cells). To determine PCa dependency on BRD7, we used shRNA-mediated knockdown of *BRD7* in all six cell lines (**Figure S11**). We observed that reduced expression of BRD7 decreased cell proliferation in AR-positive cells while having little to no effect on normal epithelial prostate cells or AR-negative PCa cells, an effect similar to, but more pronounced than what we previously observed for PBRM1 (**Figure 7D**).[31] Both 1-78 and 2-77 inhibited cell growth of LNCaP cells at all three tested concentrations (5, 1 and 0.1 µM) while being active in PC-3 only at the highest concentration (5 µM), in agreement with a greater BRD7 dependency in AR-positive PCa (**Figure 7E and 7F**). To evaluate if the activity of the compounds could be related to off-target BRD9 or BRPF1 inhibition, we treated LNCaP and PC-3 cells with BI7273 and GSK-5959 at 5, 1 and 0.1 µM and observed little to no effect with either compound (**Figure 7E and 7F**). While we previously observed a dependency on BRD9 in LNCaP cells, it required a longer incubation than 4 days, consistent with our data here.[48]

BRD7 inhibition reduces AR target gene expression. To evaluate how BRD7 BD inhibition by 2-77 affects gene expression in PCa, we performed RNA-Seq on LNCaP cells treated with 1 µM 2-77 or DMSO for 72 hours. We identified 661 genes decreased and 859 genes increased in expression with 2-77 treatment using DESeq ($p_{adj} <$ 0.05, fold change (FC) > 1.5) (**Figure 8A**). We then identified significantly enriched MSigDB_Hallmark gene sets in the differentially expressed genes. Androgen Response, G2/M checkpoint, and E2F targets were the most significantly enriched pathways in the decreased genes (**Figure 8B**), which agrees with our findings that BRD7 knockdown affects the growth and viability of only AR-positive PCa cell lines. We next performed gene set enrichment analysis (GSEA) for the Hallmark_Androgen_Response gene set using our full RNA-Seq dataset. We found significant and strong negative enrichment of androgen response genes, indicating that 2-77 treatment decreases AR target gene expression in these cells (**Figure 8C**).

To further explore the relationship between 2-77 and androgen response genes, we performed RNA-seq on LNCaP cells treated with 10 µM of the AR antagonist enzalutamide (ENZA) or DMSO for 72 hours. We identified 662 genes decreased and 609 genes increased in expression with ENZA treatment ($p_{adj} <$ 0.05, FC > 1.5) (**Figure 8D**). In agreement with a role for BRD7 in AR target gene expression, we observed a high overlap of differentially expressed genes between 2-77 and ENZA treatment, as well as a high correlation between all gene expression changes induced by treatment with 2-77 or ENZA (**Figure 8E**).

While few studies have specifically addressed the role of PBAF in PCa gene expression, several have identified universal BAF subunits or subunits from the other subcomplexes (cBAF and GBAF) to be critical for AR target gene expression.[48,51–56] Therefore, we also performed RNA-Seq with a BRG1/BRM degrader that eliminates all BAF complexes (ACBI1), a cBAF-specific inhibitor (BD98), a BRD9 degrader that eliminates GBAF complexes (dBRD9), and a PBRM1-specific BD inhibitor to target PBAF (PB16) (**Figure 8F**).[23,24,31,38] In agreement with their modes of action, we found the largest changes in gene expression with ACBI1, which eliminates all BAF

functions, and the next largest with BD98, which targets the most abundant cBAF subcomplex. In contrast, we found smaller changes in gene expression with dBRD9 or PB16, which target the less abundant GBAF and PBAF subcomplexes, respectively. In agreement with published findings, a decrease in AR target gene expression was observed for inhibitors of all three BAF subcomplexes (**Figure S12A**). Similarly, the genes differentially expressed with ENZA showed significant overlap and correlation with genes differentially expressed with the inhibitors of all three individual BAF subcomplexes (**Figure S12B**). In agreement with what we observed with 2-77, gene expression changes from PBRM1 inhibitor PB16 treatment have a particularly high correlation with gene expression changes from ENZA treatment (**Figure S12B**).

The cBAF subcomplex also facilitates gene expression driven by FOXA1, ERG and MYC, and GBAF complexes also regulate AR-independent BRD4 target genes; therefore, we hypothesized that each subcomplex would regulate a unique subset of target genes in addition to shared AR target genes.[48,51] To evaluate this, we determined the overlap of genes regulated by specific BAF subcomplex inhibitors (2-77, BD98, dBRD9, PB16) and genes regulated by ACBI1, which eliminates all three BAF subcomplexes. We observed correlation and overlap between the genes regulated by ACBI1 and the genes regulated by all four inhibitors tested, with the strongest overlaps observed for genes decreased with treatment, consistent with a general role for BAF in gene activation (**Figure S12C**). Therefore, we next compared the overlap between genes decreased with ACBI1, genes decreased with 2-77, and genes decreased with subcomplex-specific inhibitors BD98, dBRD9, or PB16 (**Figure 8G**). As expected, several genes, including AR target genes, were decreased with all drug treatments. Also, as suspected, subsets of genes decreased with ACBI1 were decreased with dBRD9 or BD98 but not 2-77, indicating subcomplex-specific inhibition of genes. In contrast, almost all genes decreased with both ACBI1 and PB16 were also decreased with 2-77, consistent with inhibition of the same subcomplex (PBAF). This trend extended to all the genes differentially regulated by PB16 and those differentially regulated by 2-77, which showed extremely high overlap and correlation (**Figure 8H**).
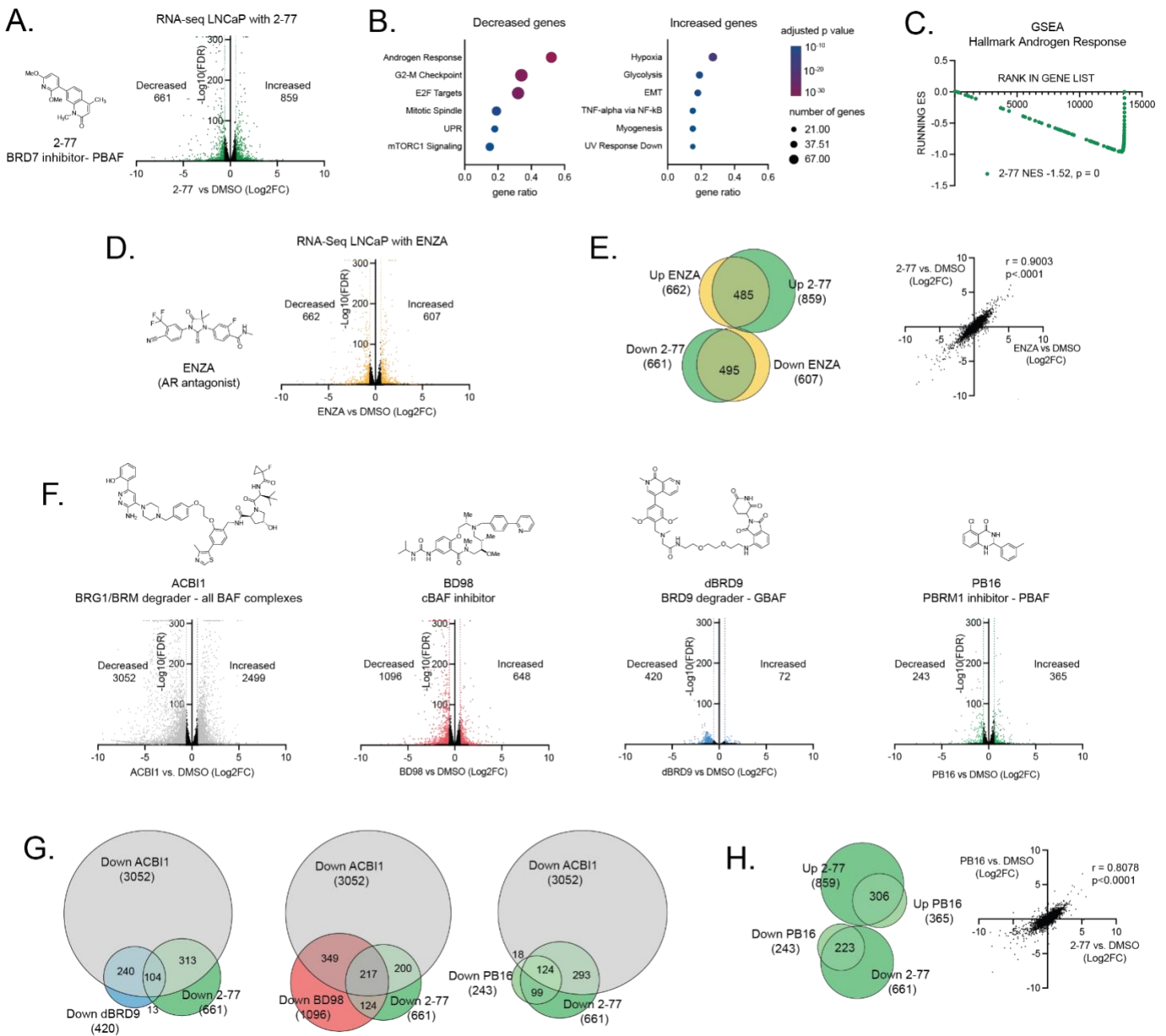
Figure 8. Gene expression analysis. **A.** Volcano plot of RNA-seq gene expression changes after treating LNCaP cells for 72 hours with 1 µM 2-77 compared to treatment with DMSO. The Log2 FC indicates the mean expression level for each gene. Each dot represents one gene. The differentially expressed genes are shown in green with p_{adj} < 0.05 and FC > 1.5. **B.** The top six most significantly enriched pathways represented in the genes significantly decreased with 2-77 treatment (**left**) and significantly increased with 2-77 treatment (**right**). **C.** GSEA analysis of RNA-Seq data from LNCaP cells treated with 2-77 using the MsigDB pathway Hallmark_Androgen_Response. **D.** RNA-seq after treating LNCaP cells for 72 hours with 10 µM ENZA or DMSO. Volcano plot of gene expression changes. The Log2 FC indicates the mean expression level for each gene. Each dot represents one gene. The differentially expressed genes are shown in yellow with p_{adj} < 0.05 and FC > 1.5. **E.** (**left**) The overlap of differentially expressed genes in LNCaP cells treated with 2-77 (green) or ENZA (yellow) and (**right**) the correlation of all gene expression changes in cells treated with ENZA (x-axis) or 2-77 (y-axis). **F.** Volcano plot of RNA-seq gene expression changes after treating LNCaP cells for 72 hours with 0.2 µM ACBI, 2 µM BD98, 0.5 µM dBRD9, or 10 µM PB16 compared to DMSO. The Log2 FC indicates the mean expression level for each gene. Each dot represents one gene. The differentially expressed genes are shown

in grey (ACBI1), red (BD98), blue (dBRD9), or light green (PB16) with padj < 0.05 and FC > 1.5. **G.** The overlap of differentially decreased ($p_{adj} < 0.05$, FC > 1.5) genes after ACBI1 (grey) 2-77 (green) and dBRD9 (blue), BD98 (red) or PB16 (light green). **H.** (**left**) The overlap of differentially expressed genes in LNCaP cells treated with 2-77 (green) or PB16 (light green), and (**right**) the correlation of all gene expression changes in cells treated with 2-77 (x-axis) or PB16 (y-axis).

CONCLUSIONS

The BAF family of chromatin remodelers has emerged as a major therapeutic target, with small molecule inhibitors and degraders of the ATPase subunits BRG1/BRM and the GBAF subunit BRD9 currently under clinical development. The PBAF subcomplex has not explicitly been validated as a therapeutic target and, as a result, significantly less effort has been invested into developing inhibitors against this subcomplex. The lack of specific PBAF inhibitors precludes a better understanding of PBAF function and its potential as a therapeutic target. To break this cycle, we require chemical tools that specifically inhibit PBAF function. In addition to the BRG1, PBAF contains two unique bromodomain-containing subunits, BRD7 and PBRM1, which, based on a recent cryo-EM structure, lie near the Histone H3 tail.[57] The second, fourth, and fifth BDs of PBRM1 (BD2, BD4, and BD5, respectively) are most critical for PBAF function by binding H3K14Ac (BD2 and BD5) and acetylated p53 (BD4), and as such, BD inhibitors have been developed for BD5 and BD2.[31,36,46,58,59] The functional role of the BD of BRD7 in PBAF is less defined. PBAF has recently been implicated in prostate and breast cancer progression through response to oxidative stress; however, the contribution of the BRD7 BD is yet to be addressed.[9,60]

Here, we report the discovery and validation of the first BRD7-selective BD inhibitor. Using structure-based drug design, we adopted structural components of BRD7/9 ligands to identify a scaffold that can occupy the BRD7 binding pocket in a unique sterically-restricted fashion. By exploiting steric interactions, we developed a ligand with significantly reduced affinity to BRD9 BD. While our scaffolds display vastly improved BRD7 selectivity over known BRD7/9 ligands, they only display slightly increased BRD7 affinity. A combination of structural biology and medicinal chemistry in the future can be used to develop inhibitors with further improved affinity and selectivity for BRD7; however, the relative instability of the BRD7 BD may be a limitation due to the entropic penalties of BRD7 binding.[26,27] The relative instability of BRD7 BD *in vitro* also makes the currently available assays for BD binding assessment challenging or impossible. To address this limitation, we developed an FP-based competition assay that eliminates confounding effects from unfolded protein and a cell-based NanoBRET competition assay. Our development of a more selective scaffold and robust biochemical assays will help further facilitate the pursuit of more potent BRD7-selective ligands. In addition, a more selective scaffold may facilitate the development of BRD7-selective PROTACs using the VHL-based BRD7/9 degrader VZ-185 as a starting point.[32]

We have also developed new cell-based assays of BRD7-dependent function. Using a series of PCa cell lines with differing BRD7 sensitivity, we identified a functional role for the BRD7 BD in facilitating AR target gene expression. We also validated BRD7 as a potential therapeutic target in AR-positive PCa. We have demonstrated that our BRD7 BD inhibitors are cellularly active and selectively inhibit PBAF function at 1 µM. These compounds can be used as tools in future efforts to understand the biochemical role of PBAF in PCa gene regulation, particularly in AR-dependent transcription. In addition, they can be used to define the therapeutic potential of targeting PBAF in additional settings, such as in chemoresistance during metastatic progression, or in sensitizing cancers to immunotherapy.[6,12,13]

EXPERIMENTAL SECTION

Binding site analysis

The binding pockets of the BD of BRD7 bound to BI9564 (PDB: 5MQ1) and the BD of BRD9 bound to BI9564 (PDB: 5F1H) were visualized and compared in the molecular visualization software PyMOL version 2.5.2

(Schrödinger®). The same software was used to analyze the binding mode of the ligands in the published crystal structures of BI7273 bound to BRD7 (PDB: 6V1E) and BRD9 (PDB: 5EU1); of BI9564 bound to BRD7 (PDB: 6V1F) and BRD9 (PDB: 5FH1); of I-BRD9 bound to BRD7 (PDB: 6V17) and BRD9 (PDB: 6V1B); of TP-472 bound to BRD7 (PDB: 6V1F) and BRD9 (PDB: 6V14); of Bromosporine bound to BRD7 (PDB: 6V1H) and BRD9 (PDB: 5IGM); and of NI-48 bound to BRPF1 (PDB: 5T4V).

Docking studies

All the molecular docking studies were performed in the Schrödinger® Maestro suite. In brief, the designated ligands were prepared using LigPrep. For the binding pose analysis, a receptor grid was generated for the crystal structures of BRD7 bound to BI7273 (PDB: 6V1E), BRD9 bound to BI7273 (PDB: 5UE1), and BRPF1 bound to NI-48 (PDB: 5T4V). The docking screening was then performed with Glide with the precision set to SP and adding the Epik state penalties to the docking score. The top poses of each ligand for each BD were visualized and analyzed in PyMOL version 2.5.2 (Schrödinger®).

Protein purification

Recombinant *N*-terminal His TEV tagged BRD7 BD (Addgene plasmid No. 98245) and N-terminal His TEV tagged BRD9 BD (Addgene plasmid No. 39012) were expressed in BL21(DE3) *E. Coli* cells with Kanamycin containing-LB broth agar. Transformed cells were incubated in Kanamycin containing-LB broth until OD_{600} reached 0.6-1, then IPTG was added to a final concentration of 1 mM. Protein expression was induced for 16 hours at 20 °C. The bacteria were then pelleted by centrifugation at 4000 × g, for 10 minutes at 4 °C and resuspended in HIS binding buffer (NaCl 150 mM, Tris 20 mM pH = 8, Imidazole 25 mM, and a Leupeptin (Cayman), Pepstatin A (Cayman) and Aprotinin (Cayman) as protease inhibitors). Cells were lysed by sonication and centrifuged at 15,000 × g for 40 minutes at 4 °C. The supernatant was incubated for 2 hours with HisPur™ Ni-NTA Resin equilibrated in the binding buffer. The beads were washed 3 times with binding buffer and the proteins were then eluted in His elution buffer (NaCl 150 mM, Tris 5 mM, Imidazole 500 mM, pH = 8, protease inhibitors as described above). SDS-PAGE was used to confirm the purity of the protein.

Thermal shift assay based on differential scanning fluorimetry

The TSA was performed following a previously reported protocol.[61] The reaction was run in 20 µL using a StepOnePlus Real-Time PCR System (Applied Biosystems). The reaction was set up in the following buffer: 10 mM HEPES pH = 7.0, 150 mM NaCl, 8× SYPRO Orange S6651 Invitrogen (5000× stock), 0.2 mg/mL His-tagged BRD7 BD or His-tagged BRD9 BD in elution buffer, 5% v/v DMSO containing the inhibitors at designated concentrations. Melting curves were obtained using a temperature gradient of 25 - 75 °C over 120 minutes with readings every 0.5 °C. Melting curves for His-tagged BRD7 BD and His-tagged BRD9 BD were obtained for four replicates at each ligand concentration and the T_m values were calculated using nonlinear least squares fit in GraphPad Prism 9.

Fluorescent polarization (FP) assay

His tagged BRD7 and BRD9 BDs were purified as described above and dialyzed in the following reaction buffer: Tris 20 mM, NaCl 150 mM, 0.02% v/v Tween 20, pH = 8.0. The assay was completed in 384-well plates (Greiner medium binding Fluotrac or Perkin Elmer Optiplate). The reaction volume was kept at 35 µL per well, and four replicates of each reaction were used. The plates were incubated and covered for 5 minutes before reading them in a Synergy Neo2 HTS multimode microplate reader (Biotek) with a xenon flash lamp as the light source. The excitation was set up at 485/20 nm, and the emission at 528/20 nm. The gain was adjusted to a blank buffer or negative control well, and the FP estimates were determined from parallel and perpendicular intensities given in millipolarization (mP) values.

The relative affinity of the BRD7 BD for the FAM-labeled probe was evaluated by direct binding as follows: starting with a concentration of 80 µM of BRD7 BD, two-fold dilutions were performed to a minimum concentration of 1.22 nM, while keeping the FAM-labeled probe concentration constant at 100 nM. The same procedure was used for the BRD9 BD but starting with a concentration of 20 µM to a minimum of 0.01 nM.

Based on the relative affinity results, 5 µM of BRD7 BD and 250 nM of BRD9 BD were used for performing the competitive assay, and the FAM-labeled probe was kept constant at 100 nM. Starting with a top concentration of 25 µM of ligand, two-fold dilutions were performed to a minimum concentration of 24.4 nM. The results of the assays were graphed in GraphPad Prism 9 and analyzed using a "One site - Specific binding" fit for the direct binding assay and a nonlinear "[Inhibitor] vs response - Variable slope (four parameters)" fit for the competitive assay.

K_i estimations based on the experimental IC_{50} were calculated employing an equation reported in the literature.[42,62] $K_i = IC_{50}/([L]_{50}/K_d + [P]_0/K_d + 1)$; where IC_{50} is the concentration of the inhibitor at 50% inhibition, $[L]_{50}$ is the concentration of free FAM-labeled probe at 50% inhibition, K_d is the dissociation constant of the protein - FAM-labeled probe complex (obtained from the direct binding assay), and $[P]_0$ is the concentration of the free protein at 0% inhibition.

BROMO*scan*™ bromodomain profiling (*bromoKd*ELECT, BromoMAX panel)

BROMO*scan*™ BD profiling was provided by Eurofins DiscoverX Corp. (San Diego, CA, USA, http://www.discoverx.com). Compounds 1-38, 1-78 and 2-77 were tested at 2 µM in a BromoMAX panel; BI7273, 1-78, and 2-77 were tested in a concentration gradient starting at a top concentration of 10 µM in a *bromoKd*ELECT assay. The results for binding interactions for the compounds are reported as % of control (DMSO).

NanoBRET assay

For the NanoBRET screening, the NanoBRET™ TE Intracellular BRD Assay-02 kit (Promega CS1810C21). NanoLuc® fusion BRD7-BD-Luc and BRD9-BD-Luc were manufactured by Promega. The assay employed HEK293T cells cultivated as described in the Cell lines section. The assay was set up in white, flat bottom, non-binding surface 96-well plates (Corning 3992), and three wells of each concentration were tested.

On the day before the assay was performed, HEK293T cells were trypsinized and collected to prepare a 15 mL suspension of 200,000 cells/mL per DNA construct in a sterile, conical tube. Lipid:DNA complexes were prepared by first preparing a 10 µg/mL solution of DNA in Opti-MEM™ without phenol red (Gibco 11058021) containing the following amounts: 9.0 µg/mL of Transfection Carrier DNA, 1.0 µg/mL NanoLuc® fusion DNA, completed to 730 µL with Opti-MEM™ without phenol red. After mixing thoroughly, 21.8 µL of FuGENE® HD (Promega E2311) were added. The solution was mixed by inversion 5 - 10 times and incubated at room temperature for 20 minutes. The Lipid:DNA mix was then added to the cell suspension and mixed by inverting 5 times. The cells mixed with lipid:DNA complex were then incubated in a 10-cm plate at least for 24 hours to allow expression.

To evaluate the relative affinity of the NanoLuc® fusion proteins for the NanoBRET Tracer, we performed a direct binding assay (**Figure S9**). Starting with a top concentration of 400 µM, two-fold dilutions of NanoBRET Tracer were performed to a concentration of 1.56 µM in DMSO to make 100× Tracer solutions. One part of 100× NanoBRET Tracer was mixed with 4 parts NanoBRET Tracer Dilution Buffer to generate 20× NanoBRET Tracer dilutions. A "no tracer" solution was prepared by mixing 1 part DMSO with 4 parts NanoBRET Tracer Dilution Buffer. The cells were then trypsinized, neutralized with regular media, and centrifuged at 250 × g for 5 minutes. The cells were then resuspended in Opti-MEM™ without phenol red, and the cell density was adjusted to 200,000 cells/mL. 68 µL of cell suspension per well were added into a white, non-binding surface, 96-well plate. 4 µL per well of each 20× NanoBRET Tracer dilution or "no tracer" solution were added to three wells containing suspended cells. The plate was then mixed on an orbital shaker for 15 seconds at 500 rpm with 1 mm of diameter

of shaking (GloMax® Discover plate reader, Promega). A 10× "no inhibitor" solution was prepared by mixing 1 part DMSO with 9 parts Opti-MEM™ without phenol red. 8 µL of "no inhibitor" dilution were added to each well. The plate was then mixed on an orbital shaker for 15 seconds at 500 rpm with 1 mm of diameter of shaking (GloMax® Discover plate reader, Promega), and incubated at 37 °C in a 5% CO_2 incubator for 2 hours. The plate was allowed to cool down to room temperature for 15 minutes before adding the 3× complete NanoBRET™ Nano-Glo® mix as described below.

Less than 2 hours before BRET measurements, the 3× complete NanoBRET™ Nano-Glo® mix was prepared in Opti-MEM™ without phenol red. This mixture consisted of a 1:166 dilution of NanoBRET™ Nano-Glo® Substrate plus a 1:500 dilution of Extracellular NanoLuc Inhibitor in Opti-MEM™ without phenol red, which were mixed gently by inversion 5-10 times in a conical tube. 40 µL of 3× complete NanoBRET™ NanoGlo® mix were added to each well and the plate was incubated for 2-3 minutes at room temperature. The donor and acceptor emissions were measured at 450 nm and 610 nm, respectively, in a SpectraMax iD5 plate reader employing the LUM-Dual Color Endpoint readout protocol, with an integration time of 1000 ms and a read height of 1 mm from the plate. The BRET ratio in mBU with background correction was calculated employing the following equation: BRET ratio = [($Acceptor_{sample}$ / $Donor_{sample}$) − ($Acceptor_{no\ tracer\ control}$ / $Donor_{no\ tracer\ control}$)] × 1000, where $Acceptor_{sample}$ and $Donor_{sample}$ are respectively the acceptor and donor emissions of each well. $Acceptor_{no\ tracer\ control}$ and $Donor_{no\ tracer\ control}$ are, respectively, the average of the acceptor and donor emissions of the three wells where the "no tracer" solution was added.

Based on the direct binding assay results, a final concentration of 0.4 µM of tracer was used for performing the competitive assay. A 100× NanoBRET Tracer solution (40 µM) was prepared in DMSO. One part of 100× NanoBRET Tracer was mixed with 4 parts NanoBRET Tracer Dilution Buffer to generate the 20× NanoBRET Tracer dilution (8 µM). A "no tracer" solution was prepared by mixing 1 part DMSO to 4 parts NanoBRET Tracer Dilution Buffer. Cells were trypsinized, centrifuged, and resuspended in Opti-MEM™, and their density was adjusted to 200,000 cells/mL as described above. 68 µL of cell suspension per well were added into a white, non-binding surface, 96-well plate. 4 µL per well of 20× NanoBRET Tracer dilution were added to wells containing suspended cells; 4 µL of "no tracer" solution was added to three wells containing suspended cells. The plate was then mixed on an orbital shaker for 15 seconds at 500 rpm with 1 mm of diameter of shaking (GloMax® Discover plate reader, Promega). Starting with a top concentration of 10 mM, two-fold dilutions of 1000× inhibitor were performed to a minimum concentration of 20 µM in DMSO. 10× solutions were prepared by mixing 1 part 1000× solution with 9 parts Opti-MEM™ without phenol red. A "no inhibitor" mixture was prepared by mixing 1 part DMSO with 9 parts Opti-MEM™ without phenol red. 8 µL of each concentration per well were added to wells containing cells with 1× tracer. For the controls, 8 µL of "no inhibitor" mixture was added to the three wells containing "no tracer" solution and three other wells containing 1× tracer. The plate was then mixed on an orbital shaker for 15 seconds at 500 rpm with 1 mm of diameter of shaking (GloMax® Discover plate reader, Promega) and incubated at 37 °C in a 5% CO_2 incubator for 2 hours. The plate was allowed to cool down to room temperature for 15 minutes before adding the 3× complete NanoBRET™ Nano-Glo® mix as described above. The donor and acceptor emissions were measured at 450 nm and 610 nm, respectively, in a SpectraMax iD5 plate reader following the protocol described above. The BRET ratio in mBU was calculated as described above, where $Acceptor_{no\ tracer\ control}$ and $Donor_{no\ tracer\ control}$ are, respectively, the average of the acceptor and donor emissions of the three wells where the "no tracer" and "no compound" solutions were added.

The results of the assays were graphed in GraphPad Prism 9 and analyzed using a nonlinear "[Agonist] vs response - Variable slope (four parameters)" fit for the direct binding assay and a nonlinear "[Inhibitor] vs response - Variable slope (four parameters)" fit for the competitive assay.

Cell lines

HEK293T (RRID:CVCL_0063), LNCaP (clone FGC; RRID:CVCL_1379), PC-3 (RRID:CVCL_0035), RWPE-1 (RRID:CVCL_3791), DU145 (RRID:CVCL_0105), 22Rv1 (RRID: CVCL_1045), and C4-2

(RRID:CVCL_4782) cells were purchased from ATCC. PC-3 cells were cultured in F12K media supplemented with 10% v/v FBS, 100 U/mL penicillin, 100 g/mL streptomycin, 2 mM L-alanyl-L-glutamine (Corning Glutagro), and 2.5 µg/mL Plasmocin (InvivoGen). HEK293T cells were cultured in DMEM media, 1 mM sodium pyruvate, and supplemented as above. LNCaP and 22Rv1 cells were cultured in RPMI-1640 with 1× MEM non-essential amino acids, 1 mM sodium pyruvate, 0.1 M HEPES (Cytiva), and supplemented as above. RWPE-1 cells were cultured in Keratinocyte SFM (Gibco 17005-042, Thermo Fisher Scientific) supplemented with 0.05 mg/mL Bovine Pituitary Extract (Gibco 13028-014), 0.005 µg/mL EGF Human Recombinant (Gibco 10450-013), 100 U/mL penicillin, 100 g/mL streptomycin, and 2.5 µg/mL Plasmocin (InvivoGen). DU145 and C4-2 cells were cultured following ATCC suggestions supplemented with 100 U/mL penicillin, 100 g/mL streptomycin, and 2.5 µg/mL Plasmocin (InvivoGen).

Cell fractionation assay

The cell fractionation assay was performed based on previously reported protocols.[17,63] After 24 hours of treatment with vehicle, I-BRD9 10 µM, 1-78 10 µM or 2-77 10 µM, 20 million HEK293T cells were harvested for processing. Cells were washed twice with cold phosphate-buffered saline and then resuspended in 500 µL of Buffer A (0.05 mM EDTA, 25 mM HEPES, 5 mM MgCl$_2$, 10% v/v glycerol, 25 mM KCl, 0.1% v/v NP40) and incubated for 8 minutes on ice. The samples were then centrifuged at 1300 × g for 5 minutes at 4 °C; supernatant 1 was collected (cytosolic fraction) and pellet 1 (nuclei) was resuspended in 500 µL of Buffer 2 (3 mM EDTA, 0.2 mM EGTA, 150 mM NaCl, 5 mM Tris, pH = 6.9). The nuclear soluble fraction was then collected after centrifugation at 20,000 × g for 15 minutes at 4 °C. The pellet (chromatin fraction) was resuspended in 500 µL of Buffer L (125 mM Tris base, 140 mM SDS, 20% v/v glycerol, 10% v/v β-mercaptoethanol, 2 mM MgCl$_2$, pH = 6.9). 2 µL of Benzonase® endonuclease were added to each sample to release the chromatin-bound proteins and the samples were then incubated shaking at 500 rpm for 16 hours at 37 °C. The supernatant containing the chromatin-bound proteins was collected for immunoblot analysis. The inhibitors were added to a final concentration of 10 µM to each buffer. DTT was added to a final concentration of 1 mM. A cocktail of protease inhibitors as described above was also added to the buffers right before each step.

For immunoblot analysis, the chromatin-bound protein samples were diluted in a 1:3 ratio with a mixture of β-mercaptoethanol and 4× Bolt™ LDS Sample Buffer (Invitrogen) in a 1:9 ratio; then boiled at 95 °C for 30 minutes to reduce viscosity. Equal volumes of the samples were loaded to the 4 - 12% SDS-polyacrylamide gel (Invitrogen).

Whole cell lysates were prepared as well for immunoblot analysis. After 24 hours of treatment with vehicle, I-BRD9 10 µM, 1-78 10 µM or 2-77 10 µM, HEK293T cells were harvested for processing. Cells were washed once with phosphate buffered saline buffer and then resuspended in RIPA buffer (50 mM Tris pH = 8, 150 mM NaCl, 1% v/v NP40, 0.1% w/v SDS, 0.5% w/v sodium deoxycholate). A cocktail of protease inhibitors was added to the buffer right before use. The samples were then incubated for 20 minutes on ice and centrifuged at 15,000 × g for 30 minutes at 4 °C. The samples were prepared for immunoblotting by mixing them in a 1:3 ratio with a mixture of β-mercaptoethanol and 4× Bolt™ LDS Sample Buffer (Invitrogen) in a 1:9 ratio, and then boiling them at 95 °C for 15 minutes. Equal amounts of protein from the samples were loaded into the 4 - 12% SDS-polyacrylamide gel (Invitrogen).

Immunoblotting

Cell lysate samples were denatured for at least 5 minutes at 95 °C, electrophoresed on 4 - 12% SDS-polyacrylamide gels (Invitrogen), and transferred onto Immobilon®-FL PVDF membranes (Millipore Sigma). The membranes were then blocked for 30 minutes in Immobilon® Signal Enhancer (Millipore Sigma) and stained overnight with primary antibodies. For secondary antibody staining, the membranes were washed with tris buffered saline buffer with 0.1% v/v Tween-20 and incubated for 1 hour with infrared-dye labeled goat anti-mouse or anti-rabbit antibodies (LICOR Biotechnology). Images were obtained using an Odyssey Clx imager (LICOR Biotechnology).

Antibodies

β-actin, Santa Cruz Biotechnology sc-47778 (1:2000); BRD7 (B-8), Santa Cruz Biotechnology sc-376180 (1:250); BRD9, Bethyl Laboratories A303-781A (1:1,000); GAPDH (6C5), Santa Cruz Biotechnology sc-32233 (1:500); Histone H3, Active Motif 39064 (1:10,000); TATA binding protein (TBP), Abcam ab818 (1:2,000).

Lentiviral production

20,000,000 HEK293T cells were cultured overnight and transfected after 16 hours with pLKO.1 puro empty vector (Addgene plasmid #8453), shBRD7-1 (TRCN0000151186), shBRD7-2 (TRCN0000154102), or shPBRM1 (TRCN0000015994) knockdown constructs in addition to the packaging vectors pMD2.G (Addgene plasmid #12259) and psPAX2 (Addgene plasmid #12260). After 16 hours of incubation the media was changed. Forty-eight hours of incubation after media change the supernatant was ultracentrifuged at 17,500 x g for 2 hours at 4 °C. The pellet was then resuspended in 200 µL phosphate-buffered saline and stored at -80 °C.

Knockdown experiments

500,000 - 600,000 cells were seeded in 6-cm plates and incubated for 24 - 72 hours such that the cells were 50 - 80% confluent before adding 5 µL of lentivirus containing pLKO.1 puro empty vector, shBRD7-1, or shBRD7-2. Twenty-four hours after transduction, the cells were selected by treatment with Puromycin (2 µg/mL) for 48 hours. Cells were then counted, seeded in a 96-well plate in a density of 5000 cells per well and incubated for 4 days. Cell viability was measured with a CellTiter-Glo® kit (Promega) in a GloMax® Discover plate reader (Promega) on day 0 and day 4. The fold increase in growth was calculated and reported relative to the empty vector control.

To evaluate the efficacy of the constructs, cells were transduced with lentivirus containing pLKO.1 puro empty vector, shBRD7-1, or shBRD7-2, and selected for 48 hours with Puromycin (2 µg/mL) after transduction. Cells were collected and resuspended in Buffer A (0.05 mM EDTA, 25 mM HEPES, 5 mM MgCl$_2$, 10% v/v glycerol, 25 mM KCl, 0.1% v/v NP40) and incubated for 15 minutes on ice. The samples were then centrifuged at $600 \times g$ for 5 minutes at 4 °C. The pellet was resuspended in Buffer B (20 mM HEPES, 150 mM NaCl, 7.5 mM MgCl$_2$, 1% v/v Triton X-100) and incubated while rotating for 30 minutes at 4 °C. A cocktail of protease inhibitors as described above was added to the buffers right before each step. The samples were then centrifuged at $10,000 \times g$ for 10 minutes at 4 °C. The protein content of the supernatant of each sample was obtained with a Pierce™ BCA Protein Assay Kit (Thermo Fisher Scientific). The samples were prepared for immunoblotting by mixing them in a 1:3 ratio with a mixture of β-mercaptoethanol and 4× Bolt™ LDS Sample Buffer (Invitrogen) in a 1:9 ratio, and then boiling them at 95 °C for 15 minutes. Equal amounts of protein from the samples were loaded into a 4 - 12% SDS-polyacrylamide gel (Invitrogen) for immunoblot analysis.

Growth inhibition experiments

Cells were seeded in a 96-well plate (no. 655098, Greiner Bio-One) with a density of 5,000 cells per well. Treatment with inhibitors at 5, 1, or 0.1 µM started the day after seeding with a final content of 0.1% v/v DMSO in the media. Media with treatment was changed every 48 hours. Cell viability was measured with a CellTiter-Glo® kit (Promega) in a GloMax® Discover plate reader (Promega) 4 days after starting the treatment and reported as a percent of DMSO control.

RNA-seq library prep and data analysis

LNCaP cells were treated in triplicate with 1 µM 2-77, 10 µM ENZA, 0.2 µM ACBI, 2 µM BD98, 10 µM PB16 or DMSO for 72 hours on 10 cm plates in RPMI growth media with 10% v/v FBS. After 72 hours of drug treatment, cells were trypsinized and RNA was extracted using TRIzol™ (Invitrogen™ - 15596026). Next, the TRIzol™-and further purified by column purification using PureLink™ Genomic RNA Mini Kit (Invitrogen™ - 12183018A) with On-column PureLink™ DNase treatment (Invitrogen™ - 12185010). The RNA quality and

concentration were determined using ThermoFisher™ Qubit fluorimetry and an Agilent™ Bioanalyzer, and all samples had a RIN score of 9.5 or greater. DNA libraries were generated using the Illumina® Stranded mRNA Prep kit (20040534) with sets of IDT® for Illumina® RNA UD Indexes (20040553) and the concentration was determined using Agilent™ Bioanalyzer. Libraries were pooled with equimolar amounts using cluster numbers obtained from MiSeq and sent for 150 bp paired-end sequencing on the NovaSeq 6000 platform (Novogene™, Sacramento, CA). Sequencing data were processed using Partek workflow. Read alignment to human genome build hg38 was performed with STAR 2.7.8a,[64] Partek E/M model was used to assemble gene level expression data from filtered alignments, and differential gene expression analysis was conducted using DESeq2.[65] Differential gene expression from LNCaP cells treated with 0.5 µM dBRD9 for 3 days was previously published.[48] Correlations were calculated using GraphPad Prism 9. Pathway analysis was performed using enrichr for 2020_MSigDB_Hallmark gene sets. Enrichments of gene sets were performed using GSEA. Quantitative overlap analysis was performed using eulerr.[66] Sequencing data were deposited into GEO with accession number: GSE228587. Reviewer token: ctyzgaiyrdqdbuf

Chemistry

Chemistry General information

All solvents and reagents, unless otherwise noted, were obtained from commercial sources and used without further purification. Reaction monitoring was done by TLC and visualized under UV light or stained with iodine, or by mass spectrometry using an Advion ExpressION CMS instrument. Columns for chromatography were prepared using silica gel 0.060-0.200 mm, 40 Å (Acros Organics). ^{1}H NMR and ^{13}C NMR data were recorded in CDCl$_3$ on a Bruker AV-III-500-HD spectrometer. NMR spectra are provided in **Figure S13**, and the results are reported as follows: chemical shift (δ) in ppm, multiplicity (s = singlet, d = doublet, t = triplet, dd = doublet of doublets, dt = doublet of triplets, m = multiplet, and br = broad signal), integration, and coupling constant (J) in hertz. Mass spectra of the small molecule inhibitors were obtained on an Agilent 1260 HPLC coupled to an Agilent 6550 Quadrupole Time-of-Flight (Q-TOF) Mass Spectrometer. All compounds are > 95% pure by HPLC.

For purification and characterization of BI-FAMa and BI-FAMb, analytical HPLC separations were completed using an Agilent 1100 system with detection at 215 nm using a water/MeCN gradient containing 0.1% v/v TFA. Preparative HPLC separations were conducted using a Varian ProStar system with detection at 215 and 254 nm using a water/MeOH gradient containing 0.1% TFA. ESI-LCMS were completed using a Waters Acquity UPLC with SQD2 mass spectrometer, equipped with a C18 reverse phase column, or an Agilent LC/MSD iQ (Agilent #G6160A, single quadrupole). Eluents of MeCN and water (each with 0.1% v/v formic acid) were used as linear gradients (% v/v MeCN in water) of: 5% to 95% (0.5 to 6 minutes), 95% to 5% (6 to 6.5 minutes), and 5% (6.5 to 7.0 minutes). Flash column chromatography was performed using Sorbent Technologies® 70 Å silica gel (40-75 µm particle size).

4-Bromo-2-methylisoquinolin-1(2*H*)-one (1)

4-bromoisoquinolin-1-ol (1 eq) was dissolved in THF (anhydrous, 10 - 15 mL) and cooled to 0 °C. Cesium carbonate (3 eq) was then added followed by methyl iodide (1.2 eq). The reaction was allowed to warm to room temperature over 16 hours, then concentrated and resuspended in DCM. The mixture was then filtered through a plug of celite and washed with DCM (2 × 20 mL) and water (2 × 20 mL). The organic layer was extracted and washed with water (3 × 20 mL) and brine (2 × 20 mL). The organic layer was then concentrated and dried to give **1**. Yield: 95%.[26]

7-Bromo-1,4-dimethylquinolin-2(1*H*)-one (2)

7-bromo-4-methylquinolin-2(1*H*)-one (1 eq) was dissolved in DMF (anhydrous, 10 - 15 mL) and cooled to 0 °C. Methyl iodide (1.2 eq) was then added followed by sodium hydride (1.3 eq). The reaction was allowed to warm

to room temperature over 16 hours and quenched with sodium hydroxide (1 M). The mixture was then diluted with water/ethyl acetate and the organic layer was extracted, dried and concentrated to give **2**. Yield: 95%.[28]

General method A: for compounds 1-38, 1-70, 1-79, and 2-88 (core 1) and 1-75 and 1-78 (core 3)

The aryl bromide (1 eq) was dissolved in DMF (anhydrous, 10 - 15 mL) under argon. Then Pd(dppf)Cl$_2$ (15%), cesium carbonate (5 eq), and the pinacol ester or boronic acid (1.2 eq) were added to the reaction flask. The reaction was stirred for 12 - 16 hours under reflux. Once completed, the mixture was filtered through a plug of celite and washed with ethyl acetate (2 × 20 mL). The filtrate was washed with water (2 × 20 mL), and brine (2 × 20 mL). The organic layer was dried with sodium sulfate anhydrous and concentrated. The resulting crude product was purified by column chromatography to yield the desired product.

Compound	Boronic acid/pinacol ester	Aryl bromide
1-38	(3,5-Dimethylphenyl)boronic acid	1
1-70	8-Methoxy-5-(4,4,5,5-tetramethyl-1,3,2-dioxaborolan-2-yl)quinoline	1
1-79	6-Methoxy-2-methyl-3-(4,4,5,5-tetramethyl-1,3,2-dioxaborolan-2-yl)pyridine	1
2-88	2,6-Dimethoxy-3-(4,4,5,5-tetramethyl-1,3,2-dioxaborolan-2-yl)pyridine	1
1-75	(3,5-Dimethylphenyl)boronic acid	2
1-78	6-Methoxy-2-methyl-3-(4,4,5,5-tetramethyl-1,3,2-dioxaborolan-2-yl)pyridine	2

4-(3,5-Dimethylphenyl)-2-methylisoquinolin-1(2*H*)-one (1-38)

Column 20-50% ethyl acetate in hexanes; yield = 35%. ^{1}H NMR (500 MHz, Chloroform-*d*) δ 8.52 (d, *J* = 7.4 Hz, 1H), 7.62 – 7.55 (m, 2H), 7.53 – 7.48 (m, 1H), 7.06 (s, 1H), 7.03 (d, *J* = 1.8 Hz, 3H), 3.65 (s, 3H), 2.38 (s, 6H). ^{13}C NMR (126 MHz, CDCl$_3$) δ 162.20, 138.23, 136.54, 136.16, 131.92, 131.27, 129.30, 128.02, 127.74, 126.82, 125.87, 124.83, 119.80, 37.03, 29.72, 21.35. HRMS calcd for C$_{18}$H$_{17}$NO [M + H]$^+$, 264.13728; found, 264.1339.

4-(8-Methoxyquinolin-5-yl)-2-methylisoquinolin-1(2*H*)-one (1-70)

Column: 20% ethyl acetate in hexanes; yield = 6.2%. ^{1}H NMR (500 MHz, CDCl$_3$) δ 8.96 (dd, *J* = 5.0, 2.7 Hz, 1H), 8.24 (dd, *J* = 8.6, 2.0 Hz, 1H), 7.51 – 7.36 (m, 7H), 7.12 (d, *J* = 2.4 Hz, 1H), 4.14 (s, 3H), 4.10 (s, 3H). HRMS calcd for C$_{20}$H$_{16}$N$_2$O$_2$ [M + H]$^+$, 317.12728; found, 317.0786.

4-(6-Methoxy-2-methylpyridin-3-yl)-2-methylisoquinolin-1(2*H*)-one (1-79)

Column: 20-30% ethyl acetate in hexanes; yield = 53%. ^{1}H NMR (500 MHz, Chloroform-*d*) δ 8.52 (d, *J* = 8.0 Hz, 1H), 7.57 (t, *J* = 8.2 Hz, 1H), 7.51 (t, *J* = 7.5 Hz, 1H), 7.40 (d, *J* = 8.3 Hz, 1H), 7.10 (d, *J* = 7.9 Hz, 1H), 6.66 (d, *J* = 8.3 Hz, 1H). ^{13}C NMR (126 MHz, CDCl$_3$) δ 163.42, 162.29, 155.87, 141.58, 136.82, 132.19, 131.91, 128.09, 127.02, 125.89, 124.57, 123.00, 116.75, 107.58, 53.51, 37.08, 22.79. HRMS calcd for C$_{17}$H$_{16}$N$_2$O$_2$ [M + H]$^+$, 281.12728; found, 281.1077.

4-(2,6-Dimethoxypyridin-3-yl)-2-methylisoquinolin-1(2*H*)-one (2-88)

Column: 20-50% ethyl acetate in hexanes; yield = 34%. ^{1}H NMR (500 MHz, Chloroform-*d*) δ 8.50 (d, *J* = 7.9 Hz, 1H), 7.56 (t, *J* = 8.1 Hz, 1H), 7.49 (t, *J* = 7.5 Hz, 1H), 7.46 (s, 1H), 7.21 (d, *J* = 7.1 Hz, 1H), 7.00 (s, 1H), 6.42

(d, $J = 7.9$ Hz, 1H), 3.99 (s, 3H), 3.88 (s, 3H), 3.64 (s, 3H). ^{13}C NMR (126 MHz, CDCl$_3$) δ 163.10, 160.74, 143.20, 136.80, 132.34, 131.75, 127.86, 126.74, 124.81, 109.71, 100.91, 53.71, 53.53, 37.07. HRMS calcd for C$_{17}$H$_{16}$N$_2$O$_3$ [M + H]$^+$, 297.12728; found, 297.1022.

7-(3,5-Dimethylphenyl)-1,4-dimethylquinolin-2(1*H*)-one (1-75)

Column: 10-30% ethyl acetate in hexanes; yield = 68%. ^{1}H NMR (500 MHz, Chloroform-*d*) δ 7.74 (d, $J = 8.2$ Hz, 1H), 7.52 (d, $J = 1.7$ Hz, 1H), 7.47 (d, $J = 9.8$ Hz, 1H), 7.26 (d, $J = 1.9$ Hz, 2H), 7.07 (s, 1H), 6.61 (d, $J = 1.4$ Hz, 1H), 3.77 (s, 3H), 2.92 (d, $J = 34.6$ Hz, 1H), 2.48 (d, $J = 1.2$ Hz, 3H), 2.42 (s, 6H), 2.33 (s, 1H). ^{13}C NMR (126 MHz, CDCl$_3$) δ 162.47, 146.44, 143.90, 140.40, 140.08, 138.64, 129.85, 125.55, 125.34, 121.34, 120.67, 120.46, 112.95, 29.42, 21.45, 18.97. HRMS calcd for C$_{19}$H$_{19}$NO [M + H]$^+$, 278.15728; found, 278.1472.

7-(6-Methoxy-2-methylpyridin-3-yl)-1,4-dimethylquinolin-2(1*H*)-one (1-78)

Column: 20-40% ethyl acetate in hexanes; yield = 45%. ^{1}H NMR (500 MHz, Chloroform-*d*) δ 7.73 (d, $J = 8.2$ Hz, 1H), 7.48 (d, $J = 8.3$ Hz, 1H), 7.20 (d, $J = 9.6$ Hz, 1H), 6.67 (d, $J = 8.3$ Hz, 1H). ^{13}C NMR (126 MHz, CDCl$_3$) δ 163.03, 162.28, 153.26, 146.24, 142.65, 140.13, 139.83, 128.93, 125.17, 123.26, 121.04, 120.27, 115.12, 107.68, 53.53, 29.30, 24.86, 23.16, 18.97. HRMS calcd for C$_{18}$H$_{18}$N$_2$O$_2$ [M + H]$^+$, 295.14728; found, 295.1236.

General method B: for compounds 2-79 (Core 1), and 2-77 and 2-81 (Core 3)

Aryl bromide (1 eq) was dissolved in 1,4-dioxane (anhydrous, 10 - 15mL), and Pd(dppf)Cl$_2$, cesium carbonate, and the pinacol ester were added. The reaction was stirred for 48 hours (2-79) or 72 hours (2-77 and 2-81) under reflux. Once completed, the mixture was filtered through a plug of celite and washed with ethyl acetate (3 × 20 mL) and DCM (1 × 25 mL). The organic layer was dried with Na$_2$SO$_4$ anhydrous and concentrated. The resulting crude product was purified by column chromatography to yield the desired product.

Compound	Pinacol ester	Aryl bromide
2-79	2-(7-Methoxynaphthalen-1-yl)-4,4,5,5-tetramethyl-1,3,2-dioxaborolane	1
2-77	2,6-Dimethoxy-3-(4,4,5,5-tetramethyl-1,3,2-dioxaborolan-2-yl)pyridine	2
2-81	2-(7-Methoxynaphthalen-1-yl)-4,4,5,5-tetramethyl-1,3,2-dioxaborolane	2

4-(2-Methoxynaphthalen-1-yl)-2-methylisoquinolin-1(2*H*)-one (2-79)

Column: 10-50% ethyl acetate in hexanes; yield = less than 15%. ^{1}H NMR (500 MHz, Chloroform-*d*) δ 7.97 (d, $J = 1.5$ Hz, 1H), 7.91 (d, $J = 1.1$ Hz, 1H), 7.88 – 7.82 (m, 2H), 7.75 (d, $J = 8.1$ Hz, 1H), 7.49 – 7.39 (m, 2H), 7.34 – 7.09 (m, 3H), 3.92 (s, 3H), 3.77 (d, $J = 1.9$ Hz, 3H). HRMS calcd for C$_{21}$H$_{17}$NO$_2$ [M + H]$^+$, 316.13728; found, 316.1093.

7-(2,6-Dimethoxypyridin-3-yl)-1,4-dimethylquinolin-2(1*H*)-one (2-77)

Column: 20-40% ethyl acetate in hexanes; yield = 47%. ^{1}H NMR (500 MHz, Chloroform-*d*) δ 7.71 (d, $J = 8.3$ Hz, 1H), 7.65 (d, $J = 8.0$ Hz, 1H), 7.54 (s, 1H), 7.41 (d, $J = 8.2$ Hz, 1H), 6.58 (s, 1H), 6.45 (d, $J = 8.0$ Hz, 1H), 3.99 (s, 6H), 3.74 (s, 3H), 2.47 (s, 3H). ^{13}C NMR (126 MHz, CDCl$_3$) δ 162.76, 159.41, 146.19, 141.55, 139.79, 139.35, 124.88, 122.93, 120.89, 120.13, 114.81, 114.72, 101.64, 53.74, 53.63, 29.31, 18.96. HRMS calcd for C$_{18}$H$_{18}$N$_2$O$_3$ [M + H]$^+$, 311.13728; found, 311.1267.

7-(2-Methoxynaphthalen-1-yl)-1,4-dimethylquinolin-2(1*H*)-one (2-81)

Column: 20-30% ethyl acetate in hexanes; yield 32%. ^{1}H NMR (500 MHz, Chloroform-d) δ 7.94 (d, J = 9.1 Hz, 1H), 7.88 – 7.82 (m, 2H), 7.47 (d, J = 6.6 Hz, 1H), 7.41 (d, J = 6.1 Hz, 2H), 7.38 – 7.34 (m, 2H), 7.29 (d, J = 8.1 Hz, 1H), 6.66 (s, 1H), 3.87 (s, 3H), 3.68 (s, 3H), 2.54 (s, 3H). ^{13}C NMR (126 MHz, CDCl$_3$) δ 162.35, 153.76, 146.43, 139.88, 139.28, 133.33, 129.81, 128.97, 128.07, 126.76, 125.03, 124.83, 124.16, 123.76, 120.98, 120.50, 117.01, 113.47, 56.67, 29.36, 24.64, 19.04. HRMS calcd for C$_{22}$H$_{19}$NO$_2$ [M + H]$^+$, 330.14728; found, 330.1244.

General method C: for compounds 2-43 and 2-63 (Core 2) and 2-70 and 2-71 (Core 4)

Step 1: Aryl aldehyde (0.5 mmol) was dissolved in THF under argon and cooled to 0 °C. The Grignard reagent (5 eq) was added dropwise over 10 minutes. The reaction was stirred till completion and allowed to warm to room temperature over 8 - 16 hours. Once the reaction was complete, the mixture was cooled to 0°C and quenched by slowly adding water. The mixture was then extracted with ethyl acetate (2 × 20 mL) where the organic fractions were collected, dried with anhydrous sodium sulfate, and concentrated. Step 2: The crude product from Step 1 was dissolved in DCM and pyridinium dichromate (3 eq) was added. The reaction was allowed to stir for 12 - 16 hours at room temperature. Following completion, the reaction mixture was flushed through a plug of celite and concentrated. The product was purified by column chromatography.

Compound	Grignard reagent	Aryl aldehyde
2-43	(3,5-Dimethylphenyl)magnesium bromide	1-methoxyisoquinoline-4-carbaldehyde
2-63	(4-Methoxy-3,5-dimethylphenyl)magnesium bromide	1-methoxyisoquinoline-4-carbaldehyde
2-70	(3,5-Dimethylphenyl)magnesium bromide	1-methyl-2-oxo-1,2-dihydroquinoline-4-carbaldehyde
2-71	(4-Methoxy-3,5-dimethylphenyl)magnesium bromide	1-methyl-2-oxo-1,2-dihydroquinoline-4-carbaldehyde

(3,5-Dimethylphenyl)(1-methoxyisoquinolin-4-yl)methanone (2-49)

Column: 5-10% ethyl acetate in hexanes; yield = 35% over two steps. ^{1}H NMR (500 MHz, Chloroform-d) δ 8.38 (d, J = 8.5 Hz, 1H), 8.34 (d, J = 7.9 Hz, 1H), 8.24 (s, 1H), 7.74 (t, J = 8.4 Hz, 1H), 7.60 (t, J = 8.1 Hz, 1H), 7.48 (s, 2H), 7.24 (s, 1H), 4.20 (s, 3H), 2.37 (s, 6H). ^{13}C NMR (126 MHz, CDCl$_3$) δ 196.45, 162.93, 145.15, 139.01, 138.09, 136.02, 134.59, 131.81, 128.05, 127.28, 125.09, 124.36, 124.02, 119.51, 54.26, 21.24. HRMS calcd for C$_{19}$H$_{17}$NO$_2$ [M + H]$^+$, 292.13728; found, 292.1099.

(4-Methoxy-3,5-dimethylphenyl)(1-methoxyisoquinolin-4-yl)methanone (2-63)

Column: 10-20% ethyl acetate in hexanes; yield = 88%. ^{1}H NMR (500 MHz, Chloroform-d) δ 8.31 (d, J = 9.4 Hz, 2H), 8.22 (s, 1H), 7.72 (t, J = 8.4 Hz, 1H), 7.58 (d, J = 15.1 Hz, 3H), 4.19 (s, 3H), 3.77 (s, 3H), 2.31 (s, 6H). ^{13}C NMR (126 MHz, CDCl$_3$) δ 195.43, 162.80, 161.26, 144.53, 136.00, 134.39, 131.72, 131.34, 131.14, 127.26, 125.02, 124.35, 124.11, 119.50, 59.72, 54.22, 16.25. HRMS calcd for C$_{20}$H$_{19}$NO$_3$ [M + H]$^+$, 322.14728; found, 322.1367.

4-(3,5-Dimethylbenzoyl)-1-methylquinolin-2(1H)-one (2-70)

Column: 20-60% ethyl acetate in hexanes; yield = 42% over two steps. ^{1}H NMR (500 MHz, Chloroform-d) δ 7.62 – 7.56 (m, 1H), 7.52 (s, 3H), 7.44 (d, J = 8.5 Hz, 1H), 7.26 (s, 1H), 7.17 (t, J = 8.1 Hz, 1H), 6.68 (s, 1H), 3.77 (s, 3H), 2.32 (s, 7H), 1.21 (s, 14H). ^{13}C NMR (126 MHz, CDCl$_3$) δ 195.11, 161.39, 147.73, 140.30, 138.69,

136.39, 135.86, 131.41, 127.96, 127.06, 122.67, 120.12, 118.25, 114.75, 77.37, 77.11, 76.86, 75.03, 29.77, 24.82, 21.16. HRMS calcd for $C_{19}H_{17}NO_2$ [M + H]$^+$, 292.13728; found, 292.115.

4-(4-Methoxy-3,5-dimethylbenzoyl)-1-methylquinolin-2(1*H*)-one (2-71)

Column: 10-30% ethyl acetate in hexanes; yield = 55% over two steps. ^{1}H NMR (500 MHz, Chloroform-*d*) δ 7.69 (d, *J* = 8.1 Hz, 1H), 7.47 (t, *J* = 7.8 Hz, 1H), 7.23 (d, *J* = 8.5 Hz, 1H), 7.13 (t, *J* = 7.5 Hz, 1H), 7.02 (d, *J* = 2.9 Hz, 3H), 6.96 (s, 1H), 6.02 (s, 1H), 3.69 (s, 2H), 3.66 (s, 3H), 3.51 (s, 3H), 2.24 (s, 3H), 2.20 (s, 6H). ^{13}C NMR (126 MHz, CDCl$_3$) δ 162.55, 156.81, 156.11, 151.08, 140.05, 139.86, 136.26, 131.29, 130.71, 130.26, 127.70, 126.23, 125.85, 122.08, 119.01, 114.61, 74.08, 72.31, 62.85, 59.67, 59.62, 36.25, 29.38, 29.33, 29.26, 16.16. HRMS calcd for $C_{20}H_{19}NO_3$ [M + H]$^+$, 322.14728; found, 322.1212.

Synthesis of BI-FAMa and BI-FAMb

Synthesis of BI-FAMa and BI-FAMb part 1
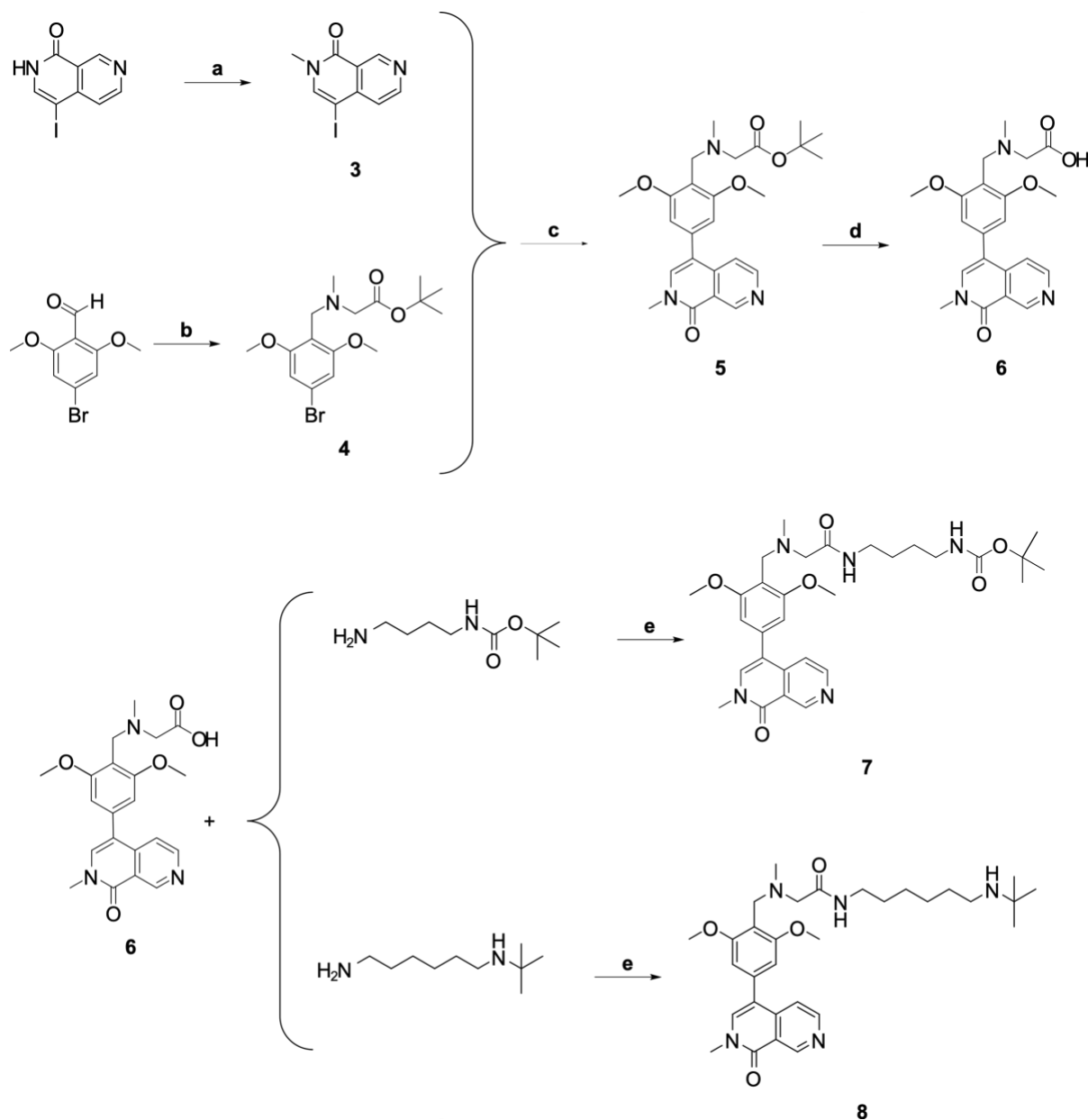
Scheme 2. Synthesis of BI-FAMa and BI-FAMb part 1.

4-iodo-2-methyl-2,7-naphthyridin-1(2*H*)-one (3)

(a) a 0.2 M solution of 4-iodo-2,7-naphthyridin-1(2*H*)-one (1 eq) in DMF was cooled down to 0°C and mixed with sodium hydride (2 eq) for 30 minutes. Iodomethane (1.6 eq) was added and the mixture was stirred at 0°C for 5 hours. Water was then added to precipitate the product which was filtered and dried to obtain a pale-yellow solid. Yield = 94%.[32]

tert-butyl 2-((2,6-dimethoxy-4-(2-methyl-1-oxo-1,2-dihydro-2,7-naphthyridin-4-yl)benzyl)(methyl)amino)acetate (4)

(b) Sarcosyl *tert*-butyl ester hydrochloride (1.5 eq) was dissolved in DCM (8 mL) with sodium acetate (1.5 eq). Acetic acid (1 eq) was added along with 4-bromo-2,6-dimethoxybenzaldehyde and the mixture was stirred for 10 minutes. Sodium triacetoxyborohydride (2 eq) was then added and the reaction was stirred for 18 hours. Once the stirring was completed, a 1 M potassium carbonate solution was added dropwise until achieving pH = 11. The mixture was extracted with DCM (4 × 10 mL), where the organic fractions were collected and washed with water (1 × 10 mL) and brine (1 × 10 mL), and dried with sodium sulfate anhydrous. The crude product was then concentrated and purified by column chromatography. Column: 0-10% ethyl acetate in hexanes; yield = 57%.[38]

tert-butyl 2-((2,6-dimethoxy-4-(2-methyl-1-oxo-1,2-dihydro-2,7-naphthyridin-4yl)benzyl)(methyl)amino)acetate (5)

(c) Compound **4** (1 eq) and bis(pinacolato)diboron were dissolved in DMF (5 mL). Potassium acetate (5 eq) and PdCl$_2$(dppf)CH$_2$Cl$_2$ were then added to the mixture. The reaction was stirred for 16 hours under reflux (90 °C), under nitrogen. Next, **3** (1eq) and 1 M potassium carbonate (2 eq) were added and the reaction was stirred under reflux (80 °C) for 16 hours. The crude product was flushed through a plug of celite and washed with DCM (3 × 50 mL). The filtrates were then washed with water (2 × 20 mL) and brine (2 × 20 mL) and dried with anhydrous magnesium sulfate. The organic fraction was concentrated, and column purified to obtain **5**. Column: 0-20% methanol in DCM. Yield = 20%.[38]

2-((2,6-dimethoxy-4-(2-methyl-1-oxo-1,2-dihydro-2,7-naphthyridin-4yl)benzyl)(methyl)amino)acetic acid (6)

(d) Compound **5** was stirred in 80% TFA in DCM at room temperature for 2 hours to obtain **6**. Yield = quantitative yield.[38]

tert-butyl (4-(2-((2,6-dimethoxy-4-(2-methyl-1-oxo-1,2-dihydro-2,7-naphthyridin-4-yl)benzyl)(methyl)amino)acetamido)butyl)carbamate (7) and *N*-(6-(tert-butylamino)hexyl)-2-((2,6-dimethoxy-4-(2-methyl-1-oxo-1,2-dihydro-2,7-naphthyridin-4-yl)benzyl)(methyl)amino)acetamide (8)

(e) Compound **6** (1 eq) was dissolved in 100 μL DMF and activated with acetic acid/DIC. Boc-1,4-diaminebutane (3 eq) or *tert*-butyl-1,6-diaminehexane (5 eq) were dissolved in 100 μL DMF and added to the mixture. The reaction was stirred for 12 - 16 hours at room temperature. The crude product was purified by HPLC to obtain **7** or **8**, respectively.

Synthesis of BI-FAMa and BI-FAMb part 2
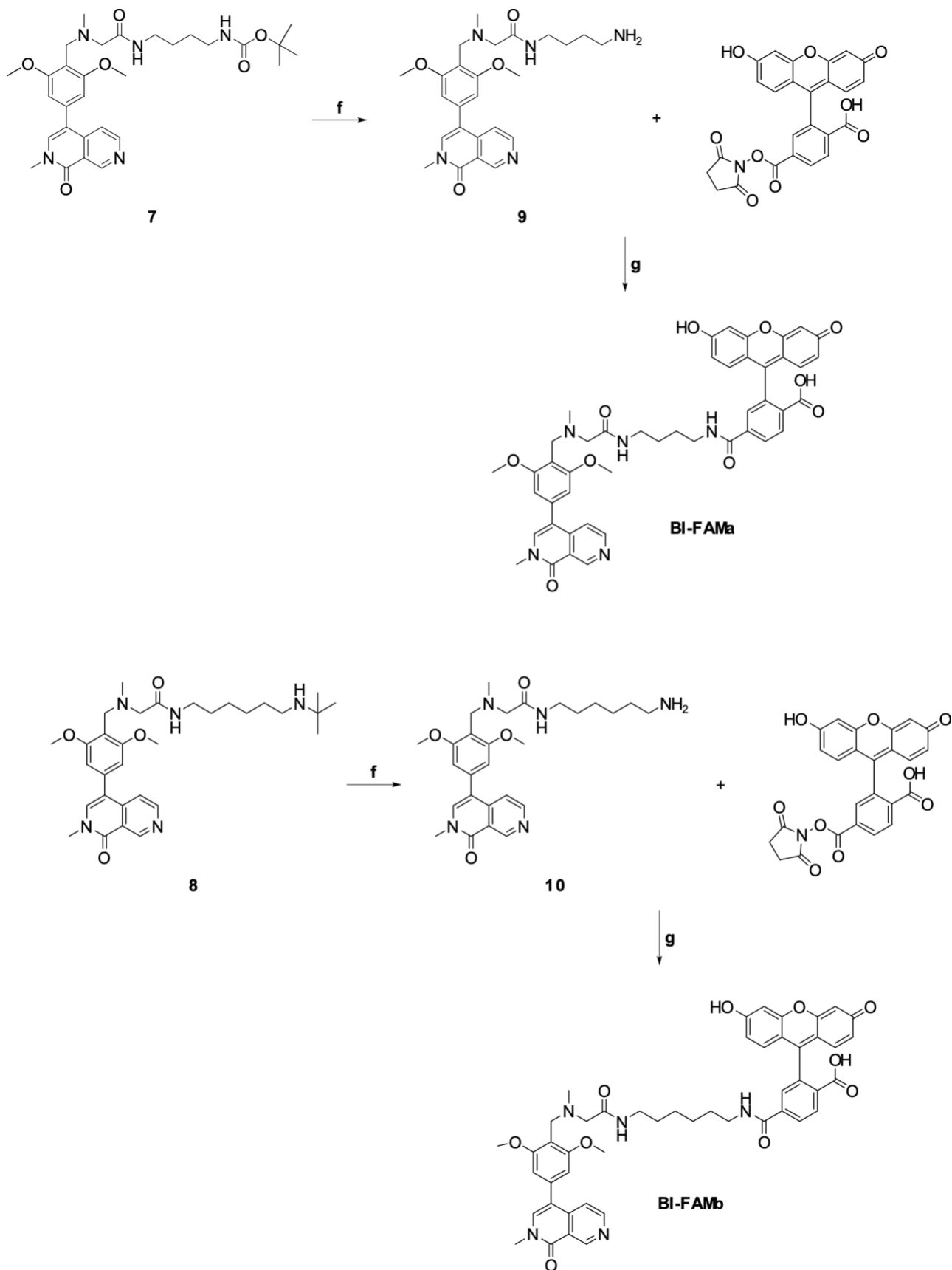
Scheme 3. Synthesis of BI-FAMa and BI-FAMb part 2.

N-(4-aminobutyl)-2-((3,5-dimethoxy-4-(2-methyl-1-oxo-1,2-dihydro-2,7-naphthyridin-4-yl)benzyl)(methyl)amino)acetamide (**9**) and N-(6-aminohexyl)-2-((3,5-dimethoxy-4-(2-methyl-1-oxo-1,2-dihydro-2,7-naphthyridin-4-yl)benzyl)(methyl)amino)acetamide (**10**)

(f) Compounds **7** or **8** were dissolved in 1 mL 75% TFA in DCM for 16 hours at room temperature. TFA was removed and the crude product was purified by HPLC to obtain **9** or **10**, respectively.

4-((4-(2-((3,5-dimethoxy-4-(2-methyl-1-oxo-1,2-dihydro-2,7-naphthyridin-4-yl)benzyl)(methyl)amino)acetamido)butyl)carbamoyl)-2-(6-hydroxy-3-oxo-3*H*-xanthen-9-yl)benzoic acid (BIFAMa) and 4-((6-(2-((3,5-dimethoxy-4-(2-methyl-1-oxo-1,2-dihydro-2,7-naphthyridin-4-yl)benzyl)(methyl)amino)acetamido)hexyl)carbamoyl)-2-(6-hydroxy-3-oxo-3H-xanthen-9-yl)benzoic acid (BI-FAMb)

(g) Compounds **9** or **10** (1 eq) and NHS-Fluorescein (5 eq) were dissolved in 500 µL of a mixture of DMSO and phosphate-buffered saline (pH = 8.2) at 1:1 ratio. The reaction was incubated without light exposure at room temperature for 4 hours. The crude product was then purified by HPLC to give BI-FAMa or BI-FAMb, respectively, which were validated by LCMS (see **Figure S14 and S15** for spectra).

SUPPORTING INFORMATION

Supp_inform.pdf: Supplementary figures, NMR spectra, and BI-FAM probes characterization.

AUTHOR INFORMATION

Corresponding author

Emily C. Dykhuizen - Department of Medicinal Chemistry and Molecular Pharmacology, Purdue Institute for Cancer Research. 201 S University St, West Lafayette, IN 47907. Email: edykhui@purdue.edu

Authors

Sandra C. Ordonez-Rubiano - Department of Medicinal Chemistry and Molecular Pharmacology, College of Pharmacy, Purdue University. Robert Heine Pharmacy Building 575 Stadium Mall Drive, West Lafayette, IN 47907. Email: sordone@purdue.edu

Chad A. Maschinot - Perfinity Biosciences Inc. 1281 Win Hentschel Blvd, West Lafayette, IN 47906. Email: cmaschinot@perfinity.com

Sijie Wang - Department of Pathology, School of Medicine, Stanford University. Edwards Bld. R341, 300 Pasteur Drive, Stanford, CA 94305-5324. Email: sijiew@stanford.edu

Surbhi Sood - Department of Medicinal Chemistry and Molecular Pharmacology, College of Pharmacy, Purdue University. Robert Heine Pharmacy Building 575 Stadium Mall Drive, West Lafayette, IN 47907. Email: sood9@purdue.edu

Brayden P. Strohmier - Department of Medicinal Chemistry and Molecular Pharmacology, College of Pharmacy, Purdue University. Robert Heine Pharmacy Building 575 Stadium Mall Drive, West Lafayette, IN 47907. Email: bstrohmi@purdue.edu

Alexander J McQuade - Department of Medicinal Chemistry and Molecular Pharmacology, College of Pharmacy, Purdue University. Robert Heine Pharmacy Building 575 Stadium Mall Drive, West Lafayette, IN 47907. Email: ajmcquad@purdue.edu

Brian C. Smith - Department of Biochemistry, Medical College of Wisconsin, 8701 Watertown Plank Rd., Milwaukee, WI 53226. Email: brismith@mcw.edu

Author contributions

S.C.O.: conceptualization, experimental design, data collection, data curation, binding site analysis, compound synthesis and characterization, docking studies, thermal shift assays, protein purification, fluorescence polarization assays, NanoBRET and cellular assays. C.M.: conceptualization, experimental design, binding site analysis, and compound rational design, synthesis, and characterization. S.W.: synthesized fluorescent probes and assisted with the fluorescence polarization assay; S.S.: RNA-seq experimental design, sample collection, and data processing and analysis; B.S.: RNA-seq sample processing and preparation of libraries; A.J.M.: assisted with thermal shift assays and growth inhibition experiments. B.C.S.: provided compound PB16. E.C.D.: conceptualization and initiation of the study, RNA-seq data analysis, funding acquisition, project supervision and administration. S.C.O. and E.C.D. wrote the manuscript with input from the other authors. All authors read and approved a final version of the manuscript before publication.

ACKNOWLEDGEMENTS

ABBREVIATIONS USED

AR, androgen receptor; Ala, alanine; Asn, asparagine; BAF, BRG1-associated factors; BD, bromodomain; BRD7, bromodomain-containing protein 7; BRD9, bromodomain-containing protein 9; BRG1, brahma related gene 1; BRM, human brahma protein; BRPF1, bromodomain and PHD finger-containing protein 1; cBAF, canonical BAF; ERG, ETS Transcription Factor ERG; ENZA, enzalutamide; FAM, fluorescein; FOXA1, Forkhead Box A1; FP, fluorescence polarization; GBAF, GLTSCR1/like-containing BAF; Glu, glutamic acid; GSEA, gene set enrichment analysis; Ile, isoleucine; Lys, lysine; mBu, milliBRET; mP, millipolarization; MYC, MYC Proto-Oncogene; PBAF, polybromo-associated BAF; PBRM1, polybromo-1; PCa, prostate cancer; Phe, phenylalanine; PROTAC, proteolysis targeting chimera; shRNA, short hairpin RNA; TSA, thermal shift assay; Tyr, tyrosine; T_m, melting temperature; Val, valine.

REFERENCES

(1) Filippakopoulos, P.; Picaud, S.; Mangos, M.; Keates, T.; Lambert, J.-P.; Barsyte-Lovejoy, D.; Felletar, I.; Volkmer, R.; Müller, S.; Pawson, T.; Gingras, A.-C.; Arrowsmith, C. H.; Knapp, S. Histone Recognition and Large-Scale Structural Analysis of the Human Bromodomain Family. *Cell* **2012**, *149* (1), 214–231. https://doi.org/10.1016/j.cell.2012.02.013.
(2) Boyson, S. P.; Gao, C.; Quinn, K.; Boyd, J.; Paculova, H.; Frietze, S.; Glass, K. C. Functional Roles of Bromodomain Proteins in Cancer. *Cancers* **2021**, *13* (14), 3606. https://doi.org/10.3390/cancers13143606.
(3) Peng, C.; Liu, H. Y.; Zhou, M.; Zhang, L. M.; Li, X. L.; Shen, S. R.; Li, G. Y. BRD7 Suppresses the Growth of Nasopharyngeal Carcinoma Cells (HNE1) through Negatively Regulating β-Catenin and ERK Pathways. *Mol Cell Biochem* **2007**, *303* (1), 141–149. https://doi.org/10.1007/s11010-007-9466-x.

(4) Liu, Y.; Zhao, R.; Wei, Y.; Li, M.; Wang, H.; Niu, W.; Zhou, Y.; Qiu, Y.; Fan, S.; Zhan, Y.; Xiong, W.; Zhou, Y.; Li, X.; Li, Z.; Li, G.; Zhou, M. BRD7 Expression and C-Myc Activation Forms a Double-Negative Feedback Loop That Controls the Cell Proliferation and Tumor Growth of Nasopharyngeal Carcinoma by Targeting Oncogenic MiR-141. *Journal of Experimental & Clinical Cancer Research* **2018**, *37* (1), 64. https://doi.org/10.1186/s13046-018-0734-2.

(5) Hu, K.; Liao, D.; Wu, W.; Han, A.-J.; Shi, H.-J.; Wang, F.; Wang, X.; Zhong, L.; Duan, T.; Wu, Y.; Cao, J.; Tang, J.; Sang, Y.; Wang, L.; Lv, X.; Xu, S.; Zhang, R.-H.; Deng, W.-G.; Li, S.-P.; Zeng, Y.-X.; Kang, T. Targeting the Anaphase-Promoting Complex/Cyclosome (APC/C)- Bromodomain Containing 7 (BRD7) Pathway for Human Osteosarcoma. *Oncotarget* **2014**, *5* (10), 3088–3100. https://doi.org/10.18632/oncotarget.1816.

(6) Niu, W.; Luo, Y.; Zhou, Y.; Li, M.; Wu, C.; Duan, Y.; Wang, H.; Fan, S.; Li, Z.; Xiong, W.; Li, X.; Li, G.; Ren, C.; Li, H.; Zhou, M. BRD7 Suppresses Invasion and Metastasis in Breast Cancer by Negatively Regulating YB1-Induced Epithelial-Mesenchymal Transition. *Journal of Experimental & Clinical Cancer Research* **2020**, *39* (1), 30. https://doi.org/10.1186/s13046-019-1493-4.

(7) Park, Y.-A.; Lee, J.-W.; Kim, H.-S.; Lee, Y.-Y.; Kim, T.-J.; Choi, C. H.; Choi, J.-J.; Jeon, H.-K.; Cho, Y. J.; Ryu, J. Y.; Kim, B.-G.; Bae, D.-S. Tumor Suppressive Effects of Bromodomain-Containing Protein 7 (BRD7) in Epithelial Ovarian Carcinoma. *Clinical Cancer Research* **2014**, *20* (3), 565–575. https://doi.org/10.1158/1078-0432.CCR-13-1271.

(8) Liang, Y.; Dong, B.; Shen, J.; Ma, C.; Ma, Z. Clinical Significance of Bromodomain-containing Protein 7 and Its Association with Tumor Progression in Prostate Cancer. *Oncol Lett* **2018**, *17* (1), 849–856. https://doi.org/10.3892/ol.2018.9665.

(9) Hagiwara, M.; Fushimi, A.; Yamashita, N.; Bhattacharya, A.; Rajabi, H.; Long, M. D.; Yasumizu, Y.; Oya, M.; Liu, S.; Kufe, D. MUC1-C Activates the PBAF Chromatin Remodeling Complex in Integrating Redox Balance with Progression of Human Prostate Cancer Stem Cells. *Oncogene* **2021**, *40* (30), 4930–4940. https://doi.org/10.1038/s41388-021-01899-y.

(10) Kikuchi, M.; Okumura, F.; Tsukiyama, T.; Watanabe, M.; Miyajima, N.; Tanaka, J.; Imamura, M.; Hatakeyama, S. TRIM24 Mediates Ligand-Dependent Activation of Androgen Receptor and Is Repressed by a Bromodomain-Containing Protein, BRD7, in Prostate Cancer Cells. *Biochimica et Biophysica Acta (BBA) - Molecular Cell Research* **2009**, *1793* (12), 1828–1836. https://doi.org/10.1016/j.bbamcr.2009.11.001.

(11) Zhao, R.; Liu, Y.; Wu, C.; Li, M.; Wei, Y.; Niu, W.; Yang, J.; Fan, S.; Xie, Y.; Li, H.; Wang, W.; Zeng, Z.; Xiong, W.; Li, X.; Li, G.; Zhou, M. BRD7 Promotes Cell Proliferation and Tumor Growth Through Stabilization of C-Myc in Colorectal Cancer. *Front Cell Dev Biol* **2021**, *9*, 659392. https://doi.org/10.3389/fcell.2021.659392.

(12) Pan, D.; Kobayashi, A.; Jiang, P.; Andrade, L. F. de; Tay, R. E.; Luoma, A. M.; Tsoucas, D.; Qiu, X.; Lim, K.; Rao, P.; Long, H. W.; Yuan, G.-C.; Doench, J.; Brown, M.; Liu, X. S.; Wucherpfennig, K. W. A Major Chromatin Regulator Determines Resistance of Tumor Cells to T Cell–Mediated Killing. *Science* **2018**, *359* (6377), 770–775. https://doi.org/10.1126/science.aao1710.

(13) Loo, C.-S.; Gatchalian, J.; Liang, Y.; Leblanc, M.; Xie, M.; Ho, J.; Venkatraghavan, B.; Hargreaves, D. C.; Zheng, Y. A Genome-Wide CRISPR Screen Reveals a Role for the Non-Canonical Nucleosome-Remodeling BAF Complex in Foxp3 Expression and Regulatory T Cell Function. *Immunity* **2020**, *53* (1), 143-157.e8. https://doi.org/10.1016/j.immuni.2020.06.011.

(14) Clapier, C. R.; Iwasa, J.; Cairns, B. R.; Peterson, C. L. Mechanisms of Action and Regulation of ATP-Dependent Chromatin-Remodelling Complexes. *Nature Reviews Molecular Cell Biology* **2017**, *18* (7), 407–422. https://doi.org/10.1038/nrm.2017.26.

(15) Mashtalir, N.; D'Avino, A. R.; Michel, B. C.; Luo, J.; Pan, J.; Otto, J. E.; Zullow, H. J.; McKenzie, Z. M.; Kubiak, R. L.; St. Pierre, R.; Valencia, A. M.; Poynter, S. J.; Cassel, S. H.; Ranish, J. A.; Kadoch, C. Modular Organization and Assembly of SWI/SNF Family Chromatin Remodeling Complexes. *Cell* **2018**, *175* (5), 1272-1288.e20. https://doi.org/10.1016/j.cell.2018.09.032.

(16)   Alpsoy, A.; Dykhuizen, E. C. Glioma Tumor Suppressor Candidate Region Gene 1 (GLTSCR1) and Its Paralog GLTSCR1-like Form SWI/SNF Chromatin Remodeling Subcomplexes. *J. Biol. Chem.* **2018**, *293* (11), 3892–3903. https://doi.org/10.1074/jbc.RA117.001065.

(17)   Gatchalian, J.; Malik, S.; Ho, J.; Lee, D.-S.; Kelso, T. W. R.; Shokhirev, M. N.; Dixon, J. R.; Hargreaves, D. C. A Non-Canonical BRD9-Containing BAF Chromatin Remodeling Complex Regulates Naive Pluripotency in Mouse Embryonic Stem Cells. *Nat Commun* **2018**, *9* (1), 5139. https://doi.org/10.1038/s41467-018-07528-9.

(18)   Wang, X.; Wang, S.; Troisi, E. C.; Howard, T. P.; Haswell, J. R.; Wolf, B. K.; Hawk, W. H.; Ramos, P.; Oberlick, E. M.; Tzvetkov, E. P.; Vazquez, F.; Hahn, W. C.; Park, P. J.; Roberts, C. W. M. BRD9 Defines a SWI/SNF Sub-Complex and Constitutes a Specific Vulnerability in Malignant Rhabdoid Tumors. *Nat Commun* **2019**, *10* (1), 1–11. https://doi.org/10.1038/s41467-019-09891-7.

(19)   Kadoch, C.; Hargreaves, D. C.; Hodges, C.; Elias, L.; Ho, L.; Ranish, J.; Crabtree, G. R. Proteomic and Bioinformatic Analysis of MSWI/SNF (BAF) Complexes Reveals Extensive Roles in Human Malignancy. *Nat Genet* **2013**, *45* (6), 592–601. https://doi.org/10.1038/ng.2628.

(20)   Schick, S.; Rendeiro, A. F.; Runggatscher, K.; Ringler, A.; Boidol, B.; Hinkel, M.; Májek, P.; Vulliard, L.; Penz, T.; Parapatics, K.; Schmidl, C.; Menche, J.; Boehmelt, G.; Petronczki, M.; Müller, A. C.; Bock, C.; Kubicek, S. Systematic Characterization of BAF Mutations Provides Insights into Intracomplex Synthetic Lethalities in Human Cancers. *Nat Genet* **2019**, 1–12. https://doi.org/10.1038/s41588-019-0477-9.

(21)   Schick, S.; Grosche, S.; Kohl, K. E.; Drpic, D.; Jaeger, M. G.; Marella, N. C.; Imrichova, H.; Lin, J.-M. G.; Hofstätter, G.; Schuster, M.; Rendeiro, A. F.; Koren, A.; Petronczki, M.; Bock, C.; Müller, A. C.; Winter, G. E.; Kubicek, S. Acute BAF Perturbation Causes Immediate Changes in Chromatin Accessibility. *Nat Genet* **2021**, *53* (3), 269–278. https://doi.org/10.1038/s41588-021-00777-3.

(22)   Iurlaro, M.; Stadler, M. B.; Masoni, F.; Jagani, Z.; Galli, G. G.; Schübeler, D. Mammalian SWI/SNF Continuously Restores Local Accessibility to Chromatin. *Nat Genet* **2021**, *53* (3), 279–287. https://doi.org/10.1038/s41588-020-00768-w.

(23)   Farnaby, W.; Koegl, M.; Roy, M. J.; Whitworth, C.; Diers, E.; Trainor, N.; Zollman, D.; Steurer, S.; Karolyi-Oezguer, J.; Riedmueller, C.; Gmaschitz, T.; Wachter, J.; Dank, C.; Galant, M.; Sharps, B.; Rumpel, K.; Traxler, E.; Gerstberger, T.; Schnitzer, R.; Petermann, O.; Greb, P.; Weinstabl, H.; Bader, G.; Zoephel, A.; Weiss-Puxbaum, A.; Ehrenhöfer-Wölfer, K.; Wöhrle, S.; Boehmelt, G.; Rinnenthal, J.; Arnhof, H.; Wiechens, N.; Wu, M.-Y.; Owen-Hughes, T.; Ettmayer, P.; Pearson, M.; McConnell, D. B.; Ciulli, A. BAF Complex Vulnerabilities in Cancer Demonstrated via Structure-Based PROTAC Design. *Nat Chem Biol* **2019**, *15* (7), 672–680. https://doi.org/10.1038/s41589-019-0294-6.

(24)   Chory, E. J.; Kirkland, J. G.; Chang, C.-Y.; D'Andrea, V. D.; Gourisankar, S.; Dykhuizen, E. C.; Crabtree, G. R. Chemical Inhibitors of a Selective SWI/SNF Function Synergize with ATR Inhibition in Cancer Cell Killing. *ACS Chem. Biol.* **2020**, *15* (6), 1685–1696. https://doi.org/10.1021/acschembio.0c00312.

(25)   Papillon, J. P. N.; Nakajima, K.; Adair, C. D.; Hempel, J.; Jouk, A. O.; Karki, R. G.; Mathieu, S.; Möbitz, H.; Ntaganda, R.; Smith, T.; Visser, M.; Hill, S. E.; Hurtado, F. K.; Chenail, G.; Bhang, H.-E. C.; Bric, A.; Xiang, K.; Bushold, G.; Gilbert, T.; Vattay, A.; Dooley, J.; Costa, E. A.; Park, I.; Li, A.; Farley, D.; Lounkine, E.; Yue, Q. K.; Xie, X.; Zhu, X.; Kulathila, R.; King, D.; Hu, T.; Vulic, K.; Cantwell, J.; Luu, C.; Jagani, Z. Discovery of Orally Active Inhibitors of Brahma Homolog (BRM)/SMARCA2 ATPase Activity for the Treatment of Brahma Related Gene 1 (BRG1)/SMARCA4-Mutant Cancers. *J. Med. Chem.* **2018**, *61* (22), 10155–10172. https://doi.org/10.1021/acs.jmedchem.8b01318.

(26)   Martin, L. J.; Koegl, M.; Bader, G.; Cockcroft, X.-L.; Fedorov, O.; Fiegen, D.; Gerstberger, T.; Hofmann, M. H.; Hohmann, A. F.; Kessler, D.; Knapp, S.; Knesl, P.; Kornigg, S.; Müller, S.; Nar, H.; Rogers, C.; Rumpel, K.; Schaaf, O.; Steurer, S.; Tallant, C.; Vakoc, C. R.; Zeeb, M.; Zoephel, A.; Pearson, M.; Boehmelt, G.; McConnell, D. Structure-Based Design of an in Vivo Active Selective BRD9 Inhibitor. *Journal of Medicinal Chemistry* **2016**, *59* (10), 4462–4475. https://doi.org/10.1021/acs.jmedchem.5b01865.

(27)   Karim, R. M.; Chan, A.; Zhu, J.-Y.; Schönbrunn, E. Structural Basis of Inhibitor Selectivity in the BRD7/9 Subfamily of Bromodomains. *J. Med. Chem.* **2020**, *63* (6), 3227–3237. https://doi.org/10.1021/acs.jmedchem.9b01980.

(28)   Clark, P. G. K.; Vieira, L. C. C.; Tallant, C.; Fedorov, O.; Singleton, D. C.; Rogers, C. M.; Monteiro, O. P.; Bennett, J. M.; Baronio, R.; Müller, S.; Daniels, D. L.; Méndez, J.; Knapp, S.; Brennan, P. E.; Dixon, D. J. LP99: Discovery and Synthesis of the First Selective BRD7/9 Bromodomain Inhibitor. *Angewandte Chemie International Edition* **2015**, *54* (21), 6217–6221. https://doi.org/10.1002/anie.201501394.

(29)   Clegg, M. A.; Bamborough, P.; Chung, C.; Craggs, P. D.; Gordon, L.; Grandi, P.; Leveridge, M.; Lindon, M.; Liwicki, G. M.; Michon, A.-M.; Molnar, J.; Rioja, I.; Soden, P. E.; Theodoulou, N. H.; Werner, T.; Tomkinson, N. C. O.; Prinjha, R. K.; Humphreys, P. G. Application of Atypical Acetyl-Lysine Methyl Mimetics in the Development of Selective Inhibitors of the Bromodomain-Containing Protein 7 (BRD7)/Bromodomain-Containing Protein 9 (BRD9) Bromodomains. *J. Med. Chem.* **2020**. https://doi.org/10.1021/acs.jmedchem.0c00075.

(30)   Mason, L. D.; Chava, S.; Reddi, K. K.; Gupta, R. The BRD9/7 Inhibitor TP-472 Blocks Melanoma Tumor Growth by Suppressing ECM-Mediated Oncogenic Signaling and Inducing Apoptosis. *Cancers* **2021**, *13* (21), 5516. https://doi.org/10.3390/cancers13215516.

(31)   Shishodia, S.; Nuñez, R.; Strohmier, B. P.; Bursch, K. L.; Goetz, C. J.; Olp, M. D.; Jensen, D. R.; Fenske, T. G.; Ordonez-Rubiano, S. C.; Blau, M. E.; Roach, M. K.; Peterson, F. C.; Volkman, B. F.; Dykhuizen, E. C.; Smith, B. C. Selective and Cell-Active PBRM1 Bromodomain Inhibitors Discovered through NMR Fragment Screening. *J Med Chem* **2022**. https://doi.org/10.1021/acs.jmedchem.2c00864.

(32)   Zoppi, V.; Hughes, S. J.; Maniaci, C.; Testa, A.; Gmaschitz, T.; Wieshofer, C.; Koegl, M.; Riching, K. M.; Daniels, D. L.; Spallarossa, A.; Ciulli, A. Iterative Design and Optimization of Initially Inactive Proteolysis Targeting Chimeras (PROTACs) Identify VZ185 as a Potent, Fast, and Selective von Hippel–Lindau (VHL) Based Dual Degrader Probe of BRD9 and BRD7. *J. Med. Chem.* **2019**, *62* (2), 699–726. https://doi.org/10.1021/acs.jmedchem.8b01413.

(33)   Wanior, M.; Preuss, F.; Ni, X.; Krämer, A.; Mathea, S.; Göbel, T.; Heidenreich, D.; Simonyi, S.; Kahnt, A. S.; Joerger, A. C.; Knapp, S. Pan-SMARCA/PB1 Bromodomain Inhibitors and Their Role in Regulating Adipogenesis. *J. Med. Chem.* **2020**, *63* (23), 14680–14699. https://doi.org/10.1021/acs.jmedchem.0c01242.

(34)   Taylor, A. M.; Bailey, C.; Belmont, L. D.; Campbell, R.; Cantone, N.; Côté, A.; Crawford, T. D.; Cummings, R.; DeMent, K.; Duplessis, M.; Flynn, M.; Good, A. C.; Huang, H.-R.; Joshi, S.; Leblanc, Y.; Murray, J.; Nasveschuk, C. G.; Neiss, A.; Poy, F.; Romero, F. A.; Sandy, P.; Tang, Y.; Tsui, V.; Zawadzke, L.; Sims, R. J. I.; Audia, J. E.; Bellon, S. F.; Magnuson, S. R.; Albrecht, B. K.; Cochran, A. G. GNE-064: A Potent, Selective, and Orally Bioavailable Chemical Probe for the Bromodomains of SMARCA2 and SMARCA4 and the Fifth Bromodomain of PBRM1. *J. Med. Chem.* **2022**, *65* (16), 11177–11186. https://doi.org/10.1021/acs.jmedchem.2c00662.

(35)   Gerstenberger, B. S.; Trzupek, J. D.; Tallant, C.; Fedorov, O.; Filippakopoulos, P.; Brennan, P. E.; Fedele, V.; Martin, S.; Picaud, S.; Rogers, C.; Parikh, M.; Taylor, A.; Samas, B.; O'Mahony, A.; Berg, E.; Pallares, G.; Torrey, A. D.; Treiber, D. K.; Samardjiev, I. J.; Nasipak, B. T.; Padilla-Benavides, T.; Wu, Q.; Imbalzano, A. N.; Nickerson, J. A.; Bunnage, M. E.; Müller, S.; Knapp, S.; Owen, D. R. Identification of a Chemical Probe for Family VIII Bromodomains through Optimization of a Fragment Hit. *J. Med. Chem.* **2016**, *59* (10), 4800–4811. https://doi.org/10.1021/acs.jmedchem.6b00012.

(36)   Myrianthopoulos, V.; Gaboriaud-Kolar, N.; Tallant, C.; Hall, M.-L.; Grigoriou, S.; Brownlee, P. M.; Fedorov, O.; Rogers, C.; Heidenreich, D.; Wanior, M.; Drosos, N.; Mexia, N.; Savitsky, P.; Bagratuni, T.; Kastritis, E.; Terpos, E.; Filippakopoulos, P.; Müller, S.; Skaltsounis, A.-L.; Downs, J. A.; Knapp, S.; Mikros, E. Discovery and Optimization of a Selective Ligand for the Switch/Sucrose Nonfermenting-Related Bromodomains of Polybromo Protein-1 by the Use of Virtual Screening and Hydration Analysis. *J Med Chem* **2016**, *59* (19), 8787–8803. https://doi.org/10.1021/acs.jmedchem.6b00355.

(37)   Mélin, L.; Gesner, E.; Attwell, S.; Kharenko, O. A.; van der Horst, E. H.; Hansen, H. C.; Gagnon, A. Design and Synthesis of LM146, a Potent Inhibitor of PB1 with an Improved Selectivity Profile over SMARCA2. *ACS Omega* 2021, *6* (33), 21327–21338. https://doi.org/10.1021/acsomega.1c01555.

(38)   Remillard, D.; Buckley, D. L.; Paulk, J.; Brien, G. L.; Sonnett, M.; Seo, H.-S.; Dastjerdi, S.; Wühr, M.; Dhe-Paganon, S.; Armstrong, S. A.; Bradner, J. E. Degradation of the BAF Complex Factor BRD9 by Heterobifunctional Ligands. *Angewandte Chemie International Edition* 2017, *56* (21), 5738–5743. https://doi.org/10.1002/anie.201611281.

(39)   Brien, G. L.; Remillard, D.; Shi, J.; Hemming, M. L.; Chabon, J.; Wynne, K.; Dillon, E. T.; Cagney, G.; Van Mierlo, G.; Baltissen, M. P.; Vermeulen, M.; Qi, J.; Fröhling, S.; Gray, N. S.; Bradner, J. E.; Vakoc, C. R.; Armstrong, S. A. Targeted Degradation of BRD9 Reverses Oncogenic Gene Expression in Synovial Sarcoma. *eLife* 2018, *7*, e41305. https://doi.org/10.7554/eLife.41305.

(40)   Hay, D. A.; Rogers, C. M.; Fedorov, O.; Tallant, C.; Martin, S.; Monteiro, O. P.; Müller, S.; Knapp, S.; Schofield, C. J.; Brennan, P. E. Design and Synthesis of Potent and Selective Inhibitors of BRD7 and BRD9 Bromodomains. *MedChemComm* 2015, *6* (7), 1381–1386. https://doi.org/10.1039/C5MD00152H.

(41)   Cochran, A. G.; Conery, A. R.; Sims, R. J. Bromodomains: A New Target Class for Drug Development. *Nat Rev Drug Discov* 2019, *18* (8), 609–628. https://doi.org/10.1038/s41573-019-0030-7.

(42)   Cer, R. Z.; Mudunuri, U.; Stephens, R.; Lebeda, F. J. IC50-to-Ki: A Web-Based Tool for Converting IC50 to Ki Values for Inhibitors of Enzyme Activity and Ligand Binding. *Nucleic Acids Research* 2009, *37* (suppl_2), W441–W445. https://doi.org/10.1093/nar/gkp253.

(43)   Wang, L.; Wang, Y.; Zhao, J.; Yu, Y.; Kang, N.; Yang, Z. Theoretical Exploration of the Binding Selectivity of Inhibitors to BRD7 and BRD9 with Multiple Short Molecular Dynamics Simulations. *RSC Advances* 2022, *12* (26), 16663–16676. https://doi.org/10.1039/D2RA02637F.

(44)   Igoe, N.; Bayle, E. D.; Fedorov, O.; Tallant, C.; Savitsky, P.; Rogers, C.; Owen, D. R.; Deb, G.; Somervaille, T. C. P.; Andrews, D. M.; Jones, N.; Cheasty, A.; Ryder, H.; Brennan, P. E.; Müller, S.; Knapp, S.; Fish, P. V. Design of a Biased Potent Small Molecule Inhibitor of the Bromodomain and PHD Finger-Containing (BRPF) Proteins Suitable for Cellular and in Vivo Studies. *J. Med. Chem.* 2017, *60* (2), 668–680. https://doi.org/10.1021/acs.jmedchem.6b01583.

(45)   Demont, E. H.; Bamborough, P.; Chung, C.; Craggs, P. D.; Fallon, D.; Gordon, L. J.; Grandi, P.; Hobbs, C. I.; Hussain, J.; Jones, E. J.; Le Gall, A.; Michon, A.-M.; Mitchell, D. J.; Prinjha, R. K.; Roberts, A. D.; Sheppard, R. J.; Watson, R. J. 1,3-Dimethyl Benzimidazolones Are Potent, Selective Inhibitors of the BRPF1 Bromodomain. *ACS Med. Chem. Lett.* 2014, *5* (11), 1190–1195. https://doi.org/10.1021/ml5002932.

(46)   Porter, E. G.; Dykhuizen, E. C. Individual Bromodomains of Polybromo-1 Contribute to Chromatin Association and Tumor Suppression in Clear Cell Renal Carcinoma. *J. Biol. Chem.* 2017, *292* (7), 2601–2610. https://doi.org/10.1074/jbc.M116.746875.

(47)   De Silva, S. M.; Dhiman, A.; Sood, S.; Mercedes, K. F.; Simmons, W. J.; Henen, M. A.; Vögeli, B.; Dykhuizen, E. C.; Musselman, C. A. PBRM1 Bromodomains Associate with RNA to Facilitate Chromatin Association. *Nucleic Acids Research* 2023, gkad072. https://doi.org/10.1093/nar/gkad072.

(48)   Alpsoy, A.; Utturkar, S. M.; Carter, B. C.; Dhiman, A.; Torregrosa-Allen, S. E.; Currie, M. P.; Elzey, B. D.; Dykhuizen, E. C. BRD9 Is a Critical Regulator of Androgen Receptor Signaling and Prostate Cancer Progression. *Cancer Res* 2021, *81* (4), 820–833. https://doi.org/10.1158/0008-5472.CAN-20-1417.

(49)   Siegel, R. L.; Miller, K. D.; Wagle, N. S.; Jemal, A. Cancer Statistics, 2023. *CA: A Cancer Journal for Clinicians* 2023, *73* (1), 17–48. https://doi.org/10.3322/caac.21763.

(50)   Wang, G.; Zhao, D.; Spring, D. J.; DePinho, R. A. Genetics and Biology of Prostate Cancer. *Genes Dev.* 2018, *32* (17–18), 1105–1140. https://doi.org/10.1101/gad.315739.118.

(51)   Xiao, L.; Parolia, A.; Qiao, Y.; Bawa, P.; Eyunni, S.; Mannan, R.; Carson, S. E.; Chang, Y.; Wang, X.; Zhang, Y.; Vo, J. N.; Kregel, S.; Simko, S. A.; Delekta, A. D.; Jaber, M.; Zheng, H.; Apel, I. J.; McMurry, L.; Su, F.; Wang, R.; Zelenka-Wang, S.; Sasmal, S.; Khare, L.; Mukherjee, S.; Abbineni, C.; Aithal, K.; Bhakta, M. S.; Ghurye, J.; Cao, X.; Navone, N. M.; Nesvizhskii, A. I.; Mehra, R.; Vaishampayan, U.;

Blanchette, M.; Wang, Y.; Samajdar, S.; Ramachandra, M.; Chinnaiyan, A. M. Targeting SWI/SNF ATPases in Enhancer-Addicted Prostate Cancer. *Nature* **2021**, 1–6. https://doi.org/10.1038/s41586-021-04246-z.

(52) Sandoval, G. J.; Pulice, J. L.; Pakula, H.; Schenone, M.; Takeda, D. Y.; Pop, M.; Boulay, G.; Williamson, K. E.; McBride, M. J.; Pan, J.; St Pierre, R.; Hartman, E.; Garraway, L. A.; Carr, S. A.; Rivera, M. N.; Li, Z.; Ronco, L.; Hahn, W. C.; Kadoch, C. Binding of TMPRSS2-ERG to BAF Chromatin Remodeling Complexes Mediates Prostate Oncogenesis. *Mol. Cell* **2018**, *71* (4), 554-566.e7. https://doi.org/10.1016/j.molcel.2018.06.040.

(53) Marshall, T. W.; Link, K. A.; Petre-Draviam, C. E.; Knudsen, K. E. Differential Requirement of SWI/SNF for Androgen Receptor Activity. *J. Biol. Chem.* **2003**, *278* (33), 30605–30613. https://doi.org/10.1074/jbc.M304582200.

(54) van de Wijngaart, D. J.; Dubbink, H. J.; Molier, M.; de Vos, C.; Trapman, J.; Jenster, G. Functional Screening of FxxLF-Like Peptide Motifs Identifies SMARCD1/BAF60a as an Androgen Receptor Cofactor That Modulates TMPRSS2 Expression. *Mol Endocrinol* **2009**, *23* (11), 1776–1786. https://doi.org/10.1210/me.2008-0280.

(55) Dai, Y.; Ngo, D.; Jacob, J.; Forman, L. W.; Faller, D. V. Prohibitin and the SWI/SNF ATPase Subunit BRG1 Are Required for Effective Androgen Antagonist-Mediated Transcriptional Repression of Androgen Receptor-Regulated Genes. *Carcinogenesis* **2008**, *29* (9), 1725–1733. https://doi.org/10.1093/carcin/bgn117.

(56) Ertl, I. E.; Brettner, R.; Kronabitter, H.; Mohr, T.; Derdak, S.; Jeitler, M.; Bilban, M.; Garstka, N.; Shariat, S. F. The SMARCD Family of SWI/SNF Accessory Proteins Is Involved in the Transcriptional Regulation of Androgen Receptor-Driven Genes and Plays a Role in Various Essential Processes of Prostate Cancer. *Cells* **2023**, *12* (1), 124. https://doi.org/10.3390/cells12010124.

(57) Yuan, J.; Chen, K.; Zhang, W.; Chen, Z. Structure of Human Chromatin-Remodelling PBAF Complex Bound to a Nucleosome. *Nature* **2022**, *605* (7908), 166–171. https://doi.org/10.1038/s41586-022-04658-5.

(58) Cai, W.; Su, L.; Liao, L.; Liu, Z. Z.; Langbein, L.; Dulaimi, E.; Testa, J. R.; Uzzo, R. G.; Zhong, Z.; Jiang, W.; Yan, Q.; Zhang, Q.; Yang, H. PBRM1 Acts as a P53 Lysine-Acetylation Reader to Suppress Renal Tumor Growth. *Nature Communications* **2019**, *10* (1), 5800. https://doi.org/10.1038/s41467-019-13608-1.

(59) Slaughter, M. J.; Shanle, E. K.; McFadden, A. W.; Hollis, E. S.; Suttle, L. E.; Strahl, B. D.; Davis, I. J. PBRM1 Bromodomains Variably Influence Nucleosome Interactions and Cellular Function. *J. Biol. Chem.* **2018**, *293* (35), 13592–13603. https://doi.org/10.1074/jbc.RA118.003381.

(60) Yamashita, N.; Morimoto, Y.; Fushimi, A.; Ahmad, R.; Bhattacharya, A.; Daimon, T.; Haratake, N.; Inoue, Y.; Ishikawa, S.; Yamamoto, M.; Hata, T.; Akiyoshi, S.; Hu, Q.; Liu, T.; Withers, H.; Liu, S.; Shapiro, G. I.; Yoshizumi, T.; Long, M. D.; Kufe, D. MUC1-C Dictates PBRM1-Mediated Chronic Induction of Interferon Signaling, DNA Damage Resistance, and Immunosuppression in Triple-Negative Breast Cancer. *Molecular Cancer Research* **2023**, *21* (3), 274–289. https://doi.org/10.1158/1541-7786.MCR-22-0772.

(61) Vivoli, M.; Novak, H. R.; Littlechild, J. A.; Harmer, N. J. Determination of Protein-Ligand Interactions Using Differential Scanning Fluorimetry. *JoVE (Journal of Visualized Experiments)* **2014**, No. 91, e51809. https://doi.org/10.3791/51809.

(62) Nikolovska-Coleska, Z.; Wang, R.; Fang, X.; Pan, H.; Tomita, Y.; Li, P.; Roller, P. P.; Krajewski, K.; Saito, N. G.; Stuckey, J. A.; Wang, S. Development and Optimization of a Binding Assay for the XIAP BIR3 Domain Using Fluorescence Polarization. *Analytical Biochemistry* **2004**, *332* (2), 261–273. https://doi.org/10.1016/j.ab.2004.05.055.

(63) Méndez, J.; Stillman, B. Chromatin Association of Human Origin Recognition Complex, Cdc6, and Minichromosome Maintenance Proteins during the Cell Cycle: Assembly of Prereplication Complexes in Late Mitosis. *Molecular and Cellular Biology* **2000**, *20* (22), 8602–8612. https://doi.org/10.1128/MCB.20.22.8602-8612.2000.

(64) Dobin, A.; Davis, C. A.; Schlesinger, F.; Drenkow, J.; Zaleski, C.; Jha, S.; Batut, P.; Chaisson, M.; Gingeras, T. R. STAR: Ultrafast Universal RNA-Seq Aligner. *Bioinformatics* **2013**, *29* (1), 15–21. https://doi.org/10.1093/bioinformatics/bts635.

(65)   Love, M. I.; Huber, W.; Anders, S. Moderated Estimation of Fold Change and Dispersion for RNA-Seq Data with DESeq2. *Genome Biol* **2014**, *15* (12), 550. https://doi.org/10.1186/s13059-014-0550-8.

(66)   Larsson, J.; Godfrey, A. Jonathan R.; Gustafsson, Peter; Eberly, David H.; Huber, Emanuel; Privé, Florian. Eulerr: Area-Proportional Euler and Venn Diagrams with Ellipses. R Package Version 7.0.0. **2022**. https://cran.r-project.org/web/packages/eulerr/index.html.

For Table Of Contents Only